Dwarf galaxies united by dark bosons

Alvaro Pozo [1,2,*] Tom Broadhurst,[1,2,3,†] George F. Smoot [1,4,5,6,7] Tzihong Chiueh,[8,9]
Hoang Nhan Luu,[1] Mark Vogelsberger,[10] and Philip Mocz[11,12]

[1]*Donostia International Physics Center (DIPC), Basque Country UPV/EHU,*
E-48080 San Sebastian, Spain
[2]*Department of Theoretical Physics, University of the Basque Country UPV/EHU, E-48080 Bilbao, Spain*
[3]*Ikerbasque, Basque Foundation for Science, E-48011 Bilbao, Spain*
[4]*WF Chao Foundation Professor, IAS, Hong Kong University of Science and Technology,*
Clear Water Bay, Kowloon 999077, Hong Kong
[5]*Energetic Cosmos Laboratory, Nazarbayev University, Nursultan, Kazakhstan*
[6]*Physics Department, University of California at Berkeley California 94720, USA*
[7]*Paris Centre for Cosmological Physics, APC, AstroParticule et Cosmologie, Université de Paris,*
CNRS/IN2P3, CEA/lrfu, Université Sorbonne Paris Cité,
10, rue Alice Domon et Leonie Duquet, 75205 Paris CEDEX 13, France
[8]*Department of Physics, National Taiwan University, Taipei 10617, Taiwan*
[9]*National Center for Theoretical Sciences, National Taiwan University, Taipei 10617, Taiwan*
[10]*Department of Physics, Kavli Institute for Astrophysics and Space Research,*
Massachusetts Institute of Technology, Cambridge, Massachusetts 02139, USA
[11]*Department of Astrophysical Sciences, Princeton University,*
4 Ivy Lane, Princeton, New Jersey 08544, USA
[12]*Lawrence Livermore National Laboratory, 7000 East Ave, Livermore, California 94550, USA*

Low-mass galaxies in the local group are dominated by dark matter and comprise the well-studied "dwarf spheroidal" (dSph) class, with typical masses of 10^9–$10^{10} M_\odot$ and also the equally numerous "ultrafaint dwarfs" (UFDs), discovered recently, that are distinctly smaller and denser with masses of only 10^7–$10^8 M_\odot$. This bimodality amongst low-mass galaxies contrasts with the scale-free continuity expected for galaxies formed under gravity, as in the standard cold dark matter model for heavy particles. Within each dwarf class we find the core radius R_c is inversely related to velocity dispersion σ, quite the opposite of standard expectations, but indicative of dark matter in a Bose-Einstein state, where the uncertainty principle requires $R_c \times \sigma$ is fixed by Planck's constant, h. The corresponding boson mass, $m_b = h/R_c\sigma$, differs by one order of magnitude between the UFD and dSph classes, with $10^{-21.4}$ eV and $10^{-20.3}$ eV, respectively. The two-boson species is reinforced by parallel relations seen between the central density and radius of UFD and dSph dwarfs, respectively, each matching the steep prediction, $\rho_c \propto R_c^{-4}$, for soliton cores in the ground state. Furthermore, soliton cores accurately fit the stellar profiles of UFD and dSph dwarfs where prominent, dense cores appear surrounded by low-density halos, as predicted by our simulations. Multiple bosons may point to a string theory interpretation for dark matter, where a discrete mass spectrum of axions is generically predicted to span many decades in mass, offering a unifying "axiverse" interpretation for the observed "diversity" of dark matter dominated dwarf galaxies.

Dark matter is commonly understood to be nonrelativistic, a characteristic necessary for its gravitational role in galaxy formation and explaining the spectrum of cosmic microwave background (CMB) fluctuations [1]. However, the conventional interpretation involving heavy particles faces challenges, such as the notable absence of new particle signatures in laboratory experiments [2,3].

Furthermore, inconsistencies arise between the predictions of cold dark matter (CDM) and the peculiar properties observed in dwarf galaxies [4–8]. Some of these issues are mitigated by addressing the missing satellite problem, but even ultrafaint dwarf (UFD) galaxies remain in tension [9]. Alternatively, the concept of dark matter as an inherently nonrelativistic Bose-Einstein condensate [10,11] has gained attention through initial simulations. These simulations reveal pervasive interference on the de Broglie wavelength within galaxies and filaments, coining the term

*[*]alvaro.pozolarrocha@bizkaia.eu
[†]tom.j.broadhurst@gmail.com

"wave dark matter" or ψDM [12,13]. In this model, bosons cannot be confined to scales smaller than the de Broglie scale, leading to the suppression of dwarf galaxy formation and the emergence of a prominent soliton core [12,14–17] in every galaxy. Here, self-gravity balances the effective pressure from the uncertainty principle in the ground state. Crucially, smaller galaxies are predicted to have wider cores and lower density because the soliton is larger at lower momentum, a hypothesis we explore in this study.

Here, we rigorously test the distinctive soliton predictions by examining well-resolved dwarf galaxies within the local group that orbit both Andromeda and the Milky Way. We utilize their star count profiles and velocity dispersion profiles (refer to the Appendix A). Initially, we plot the reported half-light radius, R_h, against the standard dynamical measure of density within this radius, $M(< R_h) \propto \sigma^2 R_h$. This allows the central density to scale to an order unity dimensionless constant α, expressed as $4\pi G \rho_h = \alpha \sigma^2 / R_h^2$. The left panel of Fig. 1 displays this correlation, color coded by stellar luminosity, revealing two steep parallel relations. UFD galaxies follow a relatively small and dense track compared to the dSph dwarfs. Both classes of dwarfs exhibit a similar, unexpectedly negative

correlation, trending towards lower density and larger radius, as illustrated in Fig. 1.

This study is built upon the premise that stars might effectively trace dark matter, a notion previously deemed controversial. Numerous distinguishing features among different dark matter models not only support this idea but also illustrate how stellar profiles should evolve uniquely in each model. In the context of cold dark matter, the scale-free formation of dark matter structures extends to extremely small scales, encompassing lower halo masses with higher DM concentrations. Conversely, ψDM inherently exhibits small-scale suppression in the power spectrum, restricting the minimum scale of structure below the de Broglie length determined by the boson mass. Consequently, structures below approximately $10^9 M_\odot$ are suppressed for a boson mass of 10^{-22} eV, aligned with the observed $\simeq 0.3$ kpc scale of dwarf galaxy cores. This limitation leads to a delayed galaxy formation in ψDM compared to CDM, resulting in a distinct evolutionary history. In CDM, the formation of the first "filamentary" structures, consisting of low-mass subhalos, occurs earlier. Conversely, in ψDM, there is no fragmentation along filaments due to the small-scale power spectrum cutoff,
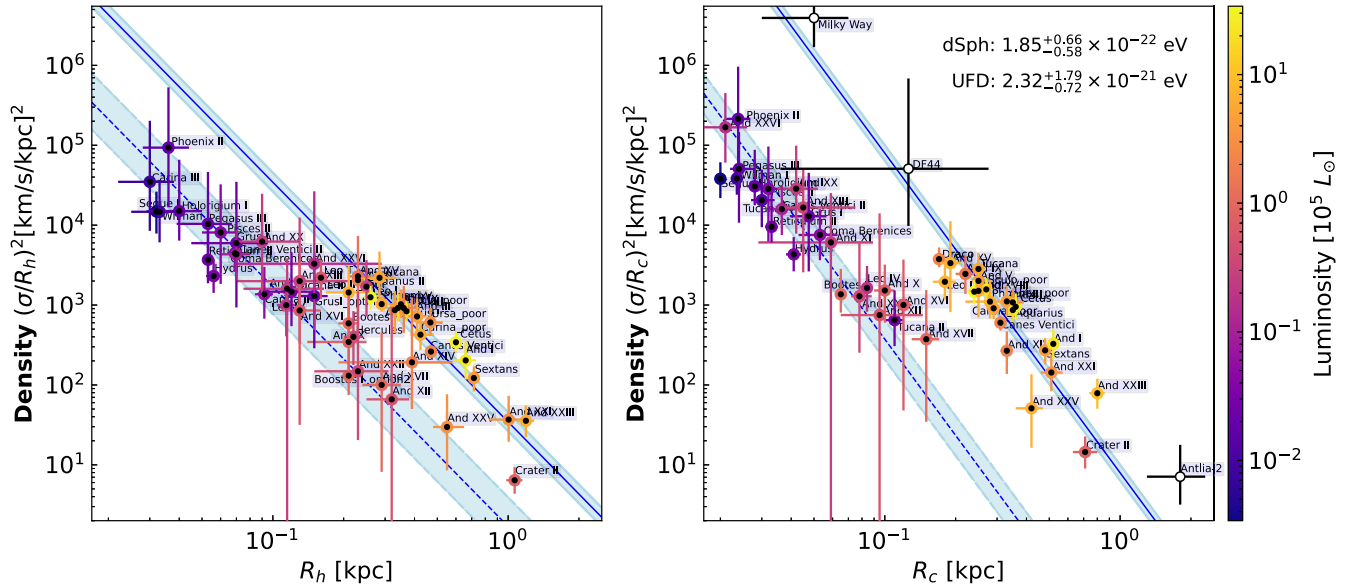

FIG. 1. (Left panel) Density vs half-light radius: Here, we plot the central density, $(\sigma/R_h)^2$, for each local dwarf (named on the plot), as reported by various groups (refer to the Appendixes A and B). These are color-coded by luminosity, revealing a clear distinction between the UFD and dSph classes. The data forms two parallel power-law fits shown in blue. (Right panel) Density vs core radius: Here, we depict the density within our fitted core radius for each dwarf, $(\sigma/R_c)^2$, utilizing the soliton form for the core (refer to the Appendix B for all individual dwarf fits to ψDM and Plummer profiles). This approach results in sharper parallel relationships between the UFD and dSph dwarfs, showing a good fit to the slope $d \log \rho_c / d \log R_c = -4$. This slope corresponds to the time-independent soliton solution of the Schrodinger-Poisson relation, where a higher soliton mass leads to a narrower core. The slopes of the blue lines are constrained to be -4, as predicted by wave dark matter. For the left panel, the slope is -3 due to the R_{half}/R_c relation. Core densities reported for the Milky Way, DF44, and Antlia-2 have been added and are seen to be consistent with the lighter boson, aligning with the dSph class. We have included core densities reported for the Milky Way, DF44, and Antlia-2, found to be consistent with the lighter boson, aligning with the dSph class. It is important to note that R_c cannot be as efficiently constrained for these cases, and thus they have been added in an illustrative manner (without accounting for the calculations), colored in white. Their values are presented without ensuring their reasonability as with the other cases.

resulting in a more continuous distribution of dark matter. Furthermore, these filaments persist for longer periods in ψDM, as the gravitational attraction from the early formation of the first halos in CDM tends to disrupt them earlier. The prolonged lifetimes of these filaments in wave dark matter favor the formation of a greater number of stars within them, leading to significant differences in the location and extent of stellar profiles in CDM and ψDM galaxies. This also causes baryonic objects to appear more diffuse or smoothed compared to CDM, suggesting their potential as excellent tracers of dark matter in ψDM [18,19].

In dSph galaxies, stellar motions are predominantly influenced by the gravitational potential of dark matter (they are much more dominated than giant galaxies and that is the main reason why are the ideal guinea pigs for this study), leading to anticipated observable differences in stars based on the nature of dark matter. The formation and early evolution of galaxies and filaments are also sensitive to the nature of dark matter, particularly influenced by the suppressed high-k power spectrum in warm dark matter $(\text{WDM})/\psi$DM models. The wave behavior and quantum pressure in ψDM result in distinct virialized DM halo structures with prominent soliton cores, contrasting with the smooth cores seen in CDM. While CDM predicts cuspy profiles [20,21], simulations of merging DM halos in ψDM clearly reveal the formation of soliton structures at the de Broglie wavelength scale [12,15,22], standing out in terms of core density above the surrounding DM halo. This differs from the early fragmentation of filaments and cuspy halos in CDM [15,18,19]. Studies by [18,19] demonstrate that baryonic feedback has limited impact on halos within the $10^9 M_\odot$ to $10^{10} M_\odot$ range for redshifts $z > 6$, failing to soften the cuspy profiles of CDM/WDM to produce cores. Consequently, neither CDM nor WDM can account for the claimed core origins from dynamical studies of dSph galaxies [23,24].

This concept has been partially explored in prior studies [15,18,19], where simulations within the ψDM framework have previously revealed the birth of stars along dense dark matter filaments, effectively tracing dark matter. This phenomenon has been emphasized as a distinctive "smoking gun" signature of ψDM [18]. Additionally, it is worth noting that our recent work [25] has further reinforced the notion that the anticipated stellar profiles from simulations for three major DM models—CDM, WDM, and ψDM— exhibit slight but meaningful distinctions, directly linked to the unique characteristics of each individual DM model. Additionally, the analysis has been extended to the relative distribution of ψDM and baryons in virialized galaxies. The conclusion is that, even though the baryonic profiles and dark matter profiles still differ, only ψDM exhibits cases where a similar distribution can be found.

The presence of prominent cores is clearly observed in the star count profiles of both ultrafaint dwarf and dwarf spheroidal galaxies, as illustrated in Fig. 2, when averaged within each class of dwarf. There is an evident difference in scale between UFD and dSph galaxies, with a radius factor of approximately 10. These cores are individually discernible in deep images, as presented in most cases (refer to the Appendix B individual fits), and they are deemed "prominent" due to the core density rising well above the surrounding "halo" by a factor of 30 in density for both classes of dwarfs, as seen in Fig. 2. The stellar cores exhibit similarity to the commonly adopted Plummer profile (depicted by the red curve in Fig. 2), but they more accurately align with the soliton form of ψDM in the ground state. This alignment is noteworthy despite the inherent parameter-free nature of the soliton profile, with the boson mass being the sole free parameter for ψDM, determining the soliton radius. Furthermore, extended halos around these solitons are observed as a general feature, extending to kiloparsec scales, consistent with recent discoveries of halos around two well-studied dwarfs [26,27]. Such extended halos are intrinsic to ψDM, composed of excited states above the ground-state soliton, as indicated by the NFW form predicted by ψDM simulations [12]. This reflects the inherently wave nature of ψDM. The averaged core-halo structure of all dSph and UFD dwarfs is presented in Fig. 2, revealing a remarkably tight agreement. All individual profiles are showcased in the Appendix B, highlighting the generality of this core-halo behavior across all well-studied dwarfs. This encompasses a typically sharp density transition between the core and the halo, as depicted in Fig. 2 and observed in most individual dwarf profiles, indicated by vertical orange bands.

The remarkable agreement with the core-halo profile of ψDM prompts the plotting of the core density versus radius relation for the soliton radius, individually measured for all dwarfs as shown in Fig. 1, where the velocity dispersion measured within that radius is also utilized. In Fig. 1, right panel, two parallel relations become more apparent for the ultrafaint Galaxy and dwarf spheroidal dwarfs, respectively, in terms of $\rho_c \propto \sigma^2/R_c^2$. For ψDM, a steep slope of $\rho_{\text{sol}} \propto R_{\text{sol}}^{-4}$ is predicted due to the volume dependence R_{sol}^{-3} and the inherent inverse scaling of the soliton radius with soliton mass, $M_{\text{sol}} \propto 1/R_{\text{sol}}$, derived from the time-independent soliton solution of the Schrödinger-Poisson coupled equation (verified by ψDM simulations [12,14]). Consequently, $\sigma^2/R_h^2 = \beta^2(\hbar/m_b)^2/R_h^4$, where β is an order unity dimensionless scaling provided by the uncertainty principle ($\hbar = m_b\sigma R_h$), resulting in a slope of $d\log\rho_{\text{sol}}/d\log R_{\text{sol}} = -4$ for ψDM. This predicted slope aligns clearly with the data in Fig. 1 (right panel) for both the ultrafaint dwarf and dwarf spheroidal galaxies. This natural alignment explains the otherwise puzzling trend where large cores within each class of dwarf have lower velocity dispersions. Notably, the "feeble giant" dwarf, Crater II, adheres to this relation, as do estimates of the core radius for the Milky Way and the ultradiffuse low-mass galaxy DF44, measuring 50 pc and 120 pc, respectively [28–30]. Importantly, this core density-radius
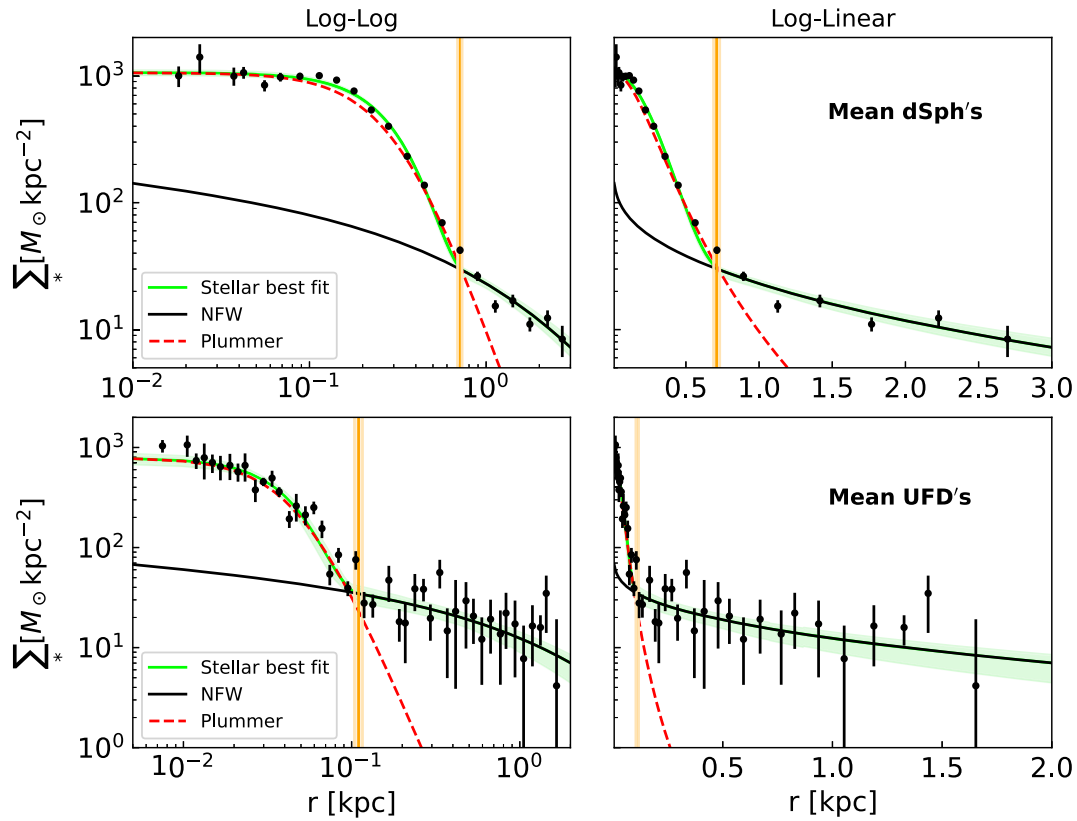
FIG. 2. (Top panel) Dwarf spheroidal galaxies: The mean star count profile, scaled to the mean core radius of all dSph dwarfs listed in Table II, reveals prominent cores in both dSph dwarfs relative to the halo, which extends to several times the core radius. While a standard Plummer profile (red dashed curve) roughly fits the core region, it falls significantly short at larger radii. In contrast, the ψDM profile, with its inherent core-halo structure, accurately fits the core from the soliton component and extends to the halo when azimuthally averaged over the excited states approximating the NFW form. The soliton profile has only one free parameter, the boson mass, m_b, determining the scale radius of the soliton. The sharp density drop between the core and the halo, by a factor of $\simeq 30$, is a characteristic feature of ψDM at a transition radius marked by the vertical orange band. The best-fit MCMC profile parameters are tabulated in Table I. (Lower panel) Ultrafaint dwarfs: The mean profile, averaged over all resolved profiles of ultrafaint dwarfs listed in Table III, exhibits the predicted ψDM core-halo structure. This includes a marked transition in density between the core (highlighted in orange), with the best-fit MCMC profile parameters tabulated in Table I.

relation remains unaffected by tidal stripping, inferred to have significantly affected Crater II and Antlia II with small pericenter orbits about the Milky Way. The stability of the soliton necessitates it always follows the inverse mass-radius relation set by the boson mass, allowing a stripped galaxy to move down the core density-radius relation without departing from it until the soliton is catastrophically destroyed by tidal forces [16]. Appendix A explains all the physics related to the wave dark matter halo, while Appendix B shows all the stellar individual density profiles of the analyzed galaxies. Additional figures, such as Figs. 5–7, expand on both panels of Fig. 1, and figures like Figs. 8 and 9 demonstrate the correlated distributions of the free parameters of Fig. 2. Additionally, Appendix B has been divided into four subsections, each presenting data related to classical dwarfs, ultra-faint dwarfs, Milky Way orbiting galaxies, and Andromeda orbiting galaxies, respectively. Figures 10–17 display the individual stellar

profiles for classical dwarfs, while 17–25 illustrate those for ultra-faint dwarfs. Versions of Fig. 2, separated by data from the Milky Way and Andromeda, are represented with Figs. 26 and 32, respectively, along with the corresponding corner plots Figs. 30 and 31 and Figs. 36 and 37. The same method has been followed to represent different versions of Fig. 3 in Figs. 27 and 33, and for Fig. 1 in Figs. 28 and 29 and 34 and 35.

Finally, we test directly for the role of the uncertainty principle to see if the inverse scaling is present between σ_c and r_c from the commutability of momentum and position required for the soliton. In Fig. 3 we see this inverse relationship is indeed supported by both the UFD and dSph dwarfs, in parallel, which is quite the opposite of the positive correlation predicted for CDM [31] where more massive dwarfs are larger, as indicated by the red curve. This agreement means we can roughly estimate the boson mass for both the UFD and dSph classes from the
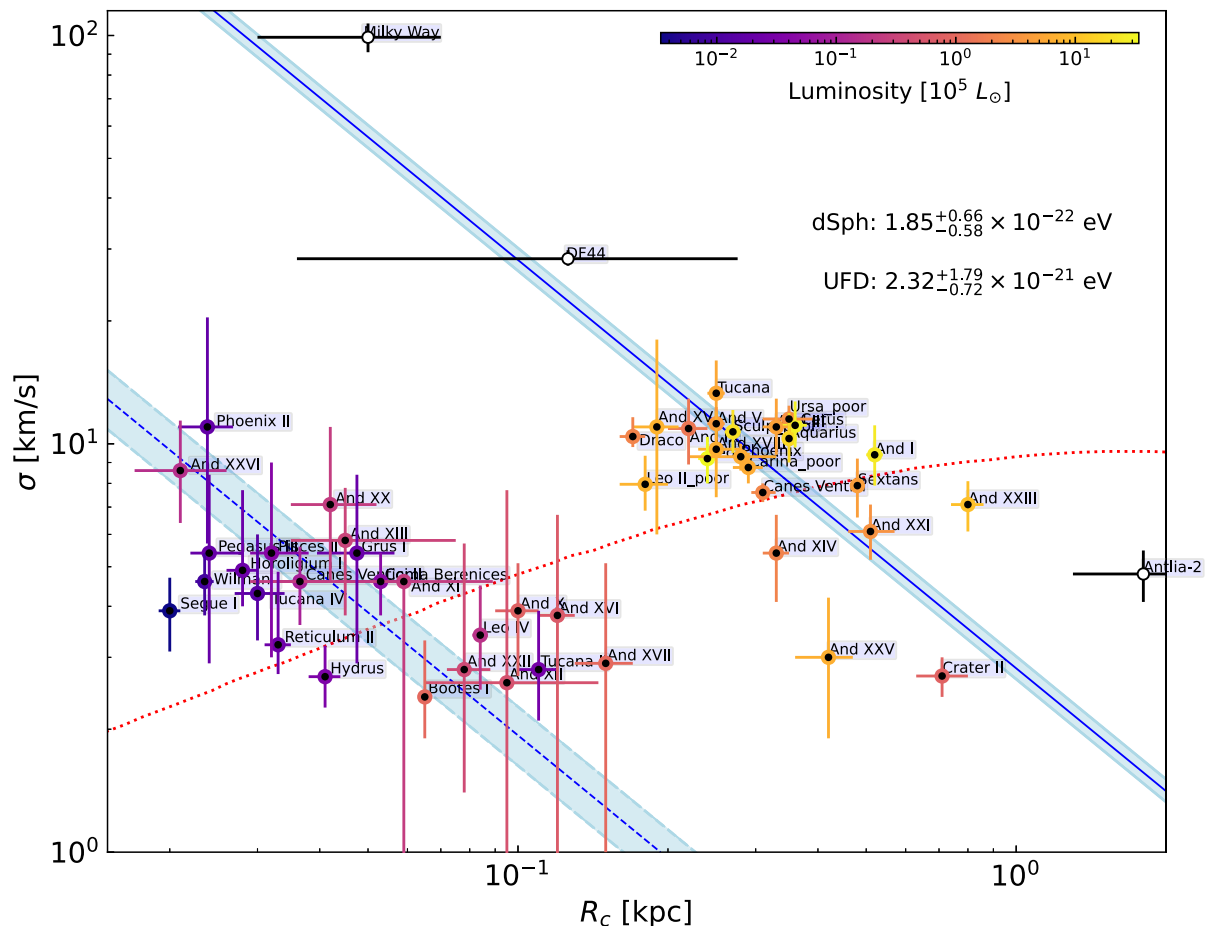
FIG. 3. Velocity dispersion vs core radius: Here, we plot the observed velocity dispersion against the core radius for all dSph and UFD dwarfs, comparing them with the inverse relation required by the uncertainty principle. The best-fit blue lines to the UFD and dSph dwarfs separately are indicated, with the corresponding boson masses of Wave-DM derived from the normalization shown in the legend. The slopes of the blue lines are constrained to be −1, as predicted by wave dark matter. Additionally, the CDM-related prediction [31] is shown as a thin red curve, where galaxies with NFW profiles are larger with increasing mass, contrary to the behavior expected in ψDM.

normalization between the core momentum $m_b \sigma_c$ and the width of the soliton standing wave so, $m_b = \hbar/2R_c\sigma_c$, fitted in Fig. 1, obtaining $m_b = 2.27^{+1.79}_{-0.65} \times 10^{-21}$ eV for the UFDs and $m_b = 1.85^{+0.66}_{-0.58} \times 10^{-22}$ eV for the dSphs, differing by an order of magnitude. This simple estimate using the uncertainty principle may be compared to individual Jeans analysis of dSph dwarfs [32], where a similar range of boson mass and core radius is derived dynamically for several dSph with high-quality profiles, in the range 0.9–2.8 × 10^{-22} eV. This estimate assumes that the stars and DM share the same spatial distribution, a reasonable assumption for stellar orbits that have relaxed over time [15,18,19,25,33], so the 3D velocity dispersion associated with the soliton wave function, where only the radial mode of kinetic energy $\langle KE \rangle_r$ is present, means in 1D we have $r_c\sigma = 0.5(\hbar/m)$, as adopted in our estimate. More precise absolute boson masses may need to rely on simulations as it is now clear that stellar orbit scattering by soliton oscillation modes affects the evolution of stellar orbits within the soliton [33]. We emphasize that irrespective of absolute values, Fig. 3 indicates there is an

order of magnitude difference in boson mass between UFD and dSph dwarfs. Furthermore, this conclusion is supported independently by the dwarfs associated with the Milky Way and with Andromeda, prefixed by "And" in Figs. 1 and 3, for which we find indistinguishable core density relations and bosons masses, as listed in Table I, thus reinforcing the generality of our two boson solution for local dwarf galaxies.

Indeed, the assertion of two distinct populations of galaxies resulting from two different boson masses can only be accurate if some aspect of the galaxy formation process leads to the spatial separation of the two types of bosons. The initial simulations and studies aimed at addressing this question are relatively recent and have not definitively clarified it. For instance, [34] conducted simulations where they analyzed the evolution of galactic halos under gravity with two different populations of bosons, major and minor. They explored scenarios with a 75% major and 25% minor composition and vice versa. The results indicated that, on large scales, the spatial distributions of filaments and massive haloes were very similar between

the two-component and single-component models, suggesting a comparable cosmological evolution that could support the coexistence of UFD and classical dwarfs. Additionally, they demonstrated how different proportions of major and minor components would affect the resulting core-halo structure. In cases where the major component dominated, a halo resulting from both bosons simultaneously would be possible. Both components contributed similarly to the soliton total density profile, resulting in a significantly lower soliton peak density than the single-component counterpart. This, along with the presence of an extended minor-component soliton, led to a much smoother soliton-to-halo transition. However, in scenarios where the minor component constituted 75% of the total population, they explicitly stated that the minor-component soliton could not form once the major-component soliton was stabilized [34]. These findings underscore that the evolution of different structures in a ψDM context is feasible even with two distinct populations of bosons, but the spatial distribution and proportion of these populations are crucial considerations. Nevertheless, it is important to mention that The referenced paper by [34] shows that if there are two ψDM components they will have different spatial distributions within a virialized halo but does not suggest that one can have different galaxies composed of different types of dark matter, which is a requirement for the objectives of this work. Unfortunately, no previous simulations have addressed this issue, making it a challenge that must be tackled in our future research.

On the other hand, there are many tensions between ψDM predictions and observational data that can potentially be alleviated by a two-field model [35]. For instance, the presence of multiple boson populations helps to smooth out the density fluctuations in ψDM haloes, thereby relaxing the constraints [36]. Additionally, a sufficiently large density fraction of the heavy field is expected to address the Lyman-α constraint [35,37].

Physically, the dominance of the heavy boson species occurs in the filament regions where the de Broglie scale of the light bosons is too large to allow fragmentation. Consequently, only low-mass halos are able to form, comprising the smaller de Broglie scale of the heavier boson (see Fig. 4). We also anticipate that the heavier galaxies formed at the nodes of filament intersection comprise approximately the initial mixture of heavy and light bosons, as depicted in Fig. 4. Simulations are underway to explore a range of boson mass ratios and relative initial boson densities (Luu *et al.* 2024, in preparation) for a quantitative comparison with the observationally distinct UFD and dSph dwarf classes. This numerical investigation poses greater challenges than those explored to date, as it must encompass the factor of 20 in boson mass ratio preferred by our analysis in this paper.

Our two boson solution for dwarf galaxies may point to the "axiverse" scenario generic to string theory [38], where in general terms a wide spectrum of axionlike scalar fields is predicted with a discrete mass spectrum spanning many decades in mass, with approximately one axion per decade.
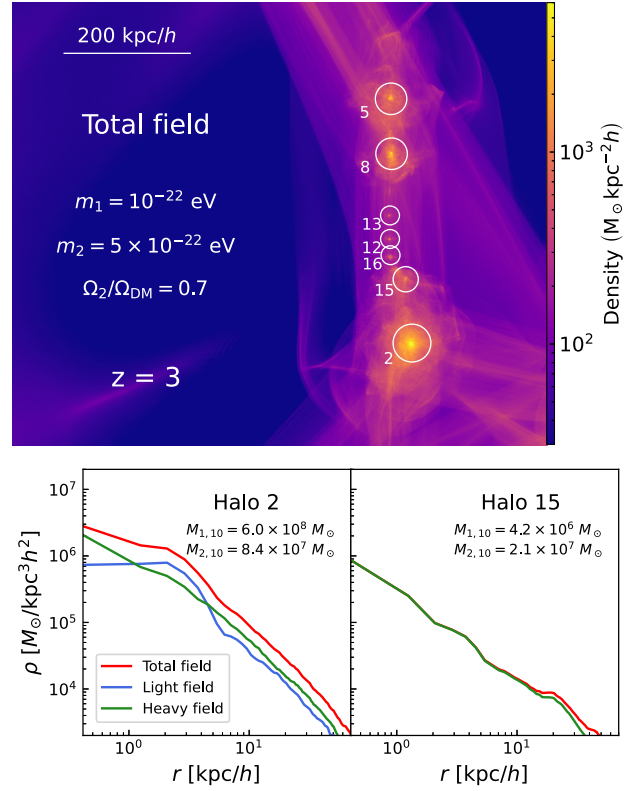

FIG. 4. Representative filament from a two-boson simulation: Low-mass galaxies mainly form within the filaments and are dominated by the heavier boson (bottom-right profile) as the relatively large de Broglie scale of the light boson prevents light boson fragmentation along filaments. The more massive halos are observed to form at the filament nodes with a mix of bosons (bottom-left profile), reflecting the equal proportion of light and heavy bosons chosen for this simulation. The boson mass ratio $m_1/m_2 = 5$ here and M_{10} denote the mass enclosed within 10 kpc of each halo.

In this context, we may infer that the proportion of the universal DM in a higher mass boson may be approximately $\sim 3\%$ compared to the lighter boson, given the factor of 10 mass difference we find, as the higher mass axion enters the

TABLE I. Profile parameters for dwarfs associated with the Milky Way and Andromeda. Column 1: Dwarf class, Column 2: Core radius r_c, Column 3: Core-halo transition radius r_t, Column 4: Number of galaxies N_{gal}, Column 5: Boson mass m_ψ.

Combinations	r_c (kpc)	r_t (kpc)	N_{gal}	m_ψ (10^{-22} eV)
dSph$_{\text{both}}$	$0.21^{+0.003}_{-0.003}$	$0.71^{+0.021}_{-0.021}$	23	$1.85^{+0.66}_{-0.58}$
UFD$_{\text{both}}$	$0.033^{+0.002}_{-0.002}$	$0.11^{+0.006}_{-0.006}$	21	$23.21^{+17.91}_{-7.23}$
dSph$_{\text{Milky Way}}$	$0.22^{+0.003}_{-0.003}$	$0.75^{+0.022}_{-0.023}$	13	$1.85^{+0.66}_{-0.58}$
dSph$_{\text{Andromeda}}$	$0.26^{+0.007}_{-0.006}$	$0.82^{+0.032}_{-0.028}$	10	$1.86^{+0.45}_{-0.53}$
UFD$_{\text{Milky Way}}$	$0.032^{+0.002}_{-0.002}$	$0.093^{+0.008}_{-0.007}$	12	$31.36^{+12.39}_{-11.57}$
UFD$_{\text{Andromeda}}$	$0.042^{+0.002}_{-0.002}$	$0.14^{+0.008}_{-0.008}$	9	$17.83^{+4.31}_{-6.73}$

horizon earlier and is redshifted to lower density ahead of lower mass axion [39]. Our two boson conclusion improves the viability of this string theory solution for DM raised in relation to the existence of UFD galaxies [40] and may relieve tension with ψDM based on excessive variance of the of the Ly-forest [41], though gas outflows and early active galactic nucleus heating must also be expected to enhance the forest variance above ideal DM simulation based predictions at some level, as too may an initially "extreme" angle scalar field for ψDM [42]. We can also now anticipate constraints on this two boson solution from JWST, where early galaxy formation related to the subdominant, heavier boson will be governed by the dominant density field of the lighter boson and hence strongly biased, favoring the formation of UFD dwarfs in groups and clusters. Alternatively, the JWST may reveal that dwarf galaxies are physically continuous at early times, as expected for scale-free CDM, implying subsequent evolutionary processes are responsible for the physical distinction between UFD and dSph dwarfs seen today.

ACKNOWLEDGMENTS

APPENDIX A: THE WAVE DARK MATTER HALO

The light bosons paradigm was first introduced by [10,43], and [11], and subsequently reconsidered with the first simulations [12,16,17,37,44–46] and in relation to the puzzling properties of dwarf spheroidal galaxies. In the simplest version, without self-interaction, the boson mass, m_b, is the only free parameter, with a fiducial value of 10^{-22} eV adopted to match the approximate kpc scale commonly reported for dark matter dominated dwarf galaxy cores.

The first simulations in this context have revealed a surprisingly rich wavelike structure with a solitonic standing wave core, surrounded by a halo of interference that is fully modulated on the de Broglie scale [12]. The solitonic core corresponds to the ground-state solution of the coupled Schrödinger-Poisson equations, with a cored density profile well-approximated by [12,14]

$$\rho_c(r) \sim \frac{1.9 a^{-1} (m_\psi/10^{-23}\text{ eV})^{-2} (r_c/\text{kpc})^{-4}}{[1 + 9.1 \times 10^{-2} (r/r_c)^2]^8} M_\odot \text{pc}^{-3}, \quad \text{(A1)}$$

Here m_ψ is the boson mass, and r_c is the solitonic core radius, which simulations show scales as halo mass [14] in the following way:

$$r_c \propto m_\psi^{-1} M_{\text{halo}}^{-1/3}, \quad \text{(A2)}$$

$$r_c = 1.6 \left(\frac{10^{-22}}{m_\psi} \text{eV} \right) a^{1/2} \left(\frac{\zeta(z)}{\zeta(0)} \right)^{-1/6} \left(\frac{M_h}{10^9 M_\odot} \right)^{-1/3} \text{ kpc.} \quad \text{(A3)}$$

Core masses of constant density scale as $\rho_c \propto (\sigma/r_c)^2$ and in the context of ψDM there is also an inverse relationship between soliton core mass and soliton radius relation required by the nonlinear solution to the Schrodinger-Poisson equation [12] so the soliton's density scales more steeply than the volume with radius, i.e. $\rho_c \propto r_c^{-4}$. The radius of the soliton is given approximately by the de Broglie wavelength $\lambda_B = \frac{h}{p}$, following from the uncertainty principle $\Delta x \Delta p \geq \frac{\hbar}{2}$, where Δx, the position dispersion given by the soliton width, $2 \times r_c$, and the dispersion in momentum Δp, given approximately by $m_b \sigma$, the product of the boson mass and the velocity dispersion of stars as tracer particles of the dominant DM potential. This allows us to determine the boson mass that corresponds to the de Broglie wavelength, $m_\psi \simeq \hbar/4 r_c \sigma_{\text{los}}$.

The simulations also show the soliton core is surrounded by an extended halo of density fluctuations on the de Broglie scale that arise by self-interference of the wave function [12] and is "hydrogenic" in form [37,47]. These cellular fluctuations are large, with full density modulation on the de Broglie scale [12] that modulate the amplitude of the Compton frequency oscillation of the coherent bosonic field, allowing a direct detection via pulsar timing [28,48].

This extended halo region, when azimuthally averaged, is found to follow the Navarro-Frank-White (NFW) density profile [12,14,20,49] so that the full radial profile may be approximated as

$$\rho_{\text{DM}}(r) = \begin{cases} \rho_c(x) & \text{if } r < X r_c, \\ \frac{\rho_0}{\frac{r}{r_s}(1 + \frac{r}{r_s})^2} & \text{otherwise,} \end{cases} \quad \text{(A4)}$$

where ρ_0 is chosen such that the inner solitonic profile matches the outer NFW-like profile at approximately $\simeq X r_c$, and r_s is the scale radius.

In this context, we can now predict the corresponding velocity dispersion profile by solving the spherically symmetric Jeans equation:

$$\frac{d(\rho_*(r)\sigma_r^2(r))}{dr} = -\rho_*(r)\frac{d\Phi_{\text{DM}}(r)}{dr} - 2\beta\frac{\rho_*(r)\sigma_r^2(r)}{r}, \quad \text{(A5)}$$

where $\rho_*(r)$ is the stellar density distribution is the stellar density distribution defined by the solitonic wave dark matter profile:

$$\rho_*(r) = \begin{cases} \rho_{1*}(r) & \text{if } r < r_t, \\ \frac{\rho_{02*}}{\frac{r}{r_{s*}}(1 + \frac{r}{r_{s*}})^2} & \text{otherwise,} \end{cases} \quad \text{(A6)}$$

where

$$\rho_{1*}(r) = \frac{\rho_{0*}}{[1 + 9.1 \times 10^{-2}(r/r_c)^2]^8} N_* \text{ kpc}^{-3}. \quad \text{(A7)}$$

Here, r_{s*} is the 3D scale radius of the stellar halo corresponding to ρ_{0*} the central stellar density, ρ_{02*} is the normalization of ρ_{0*} at the transition radius and the transition radius, r_t, is the point where the soliton structure ends and the halo begins at the juncture of the core and halo profiles. β is the anisotropy parameter, defined as [see [50], Eq. (4.61)]

$$\beta = 1 - \frac{\sigma_t^2}{\sigma_r^2}. \quad \text{(A8)}$$

Thus, the gravitational potential is given by

$$d\Phi_{\text{DM}}(r) = G\frac{M_{\text{DM}}(r)}{r^2} dr, \quad \text{(A9)}$$

with a boundary condition $\Phi_{\text{DM}}(\infty) = 0$, and the mass enclosed in a sphere of radius r is computed as follows:

$$M_{\text{DM}}(r) = 4\pi \int_0^r x^2 \rho_{\text{DM}}(x)dx. \quad \text{(A10)}$$

Finally, to directly compare our predicted dispersion velocity profile with the observations, we have to project the solution of the Jeans equation along the line of sight as follows:

$$\sigma_{\text{los}}^2(R) = \frac{2}{\Sigma(R)} \int_R^\infty \left(1 - \beta\frac{R^2}{r^2}\right) \frac{\sigma_r^2(r)\rho_*(r)}{(r^2 - R^2)^{1/2}} rdr, \quad \text{(A11)}$$

where

$$\Sigma(R) = 2 \int_R^\infty \rho_*(r)(r^2 - R^2)^{-1/2} rdr. \quad \text{(A12)}$$

APPENDIX B: DATA ANALYSIS AND RESULTS

Here, we present the stellar density profiles of a comprehensive sample of dSph and UFD dwarfs, which we compare with the generic ψDM core-halo profile outlined in Section A [Eq. (A6)]. As is evident in all the figures in Secs. B 1 and B 2, these dwarfs indeed exhibit a distinct common form–a core-halo structure similar to what is predicted for ψDM. The cores consistently adhere to the unique soliton form in cases with deep star counts. Additionally, the azimuthally averaged outer region at a larger radius is well-fitted by the NFW profile, as anticipated for ψDM [12]. The core and halo regimes are easily distinguishable, as the core exhibits higher density compared to the halo. The transition radius is marked by an orange vertical line in the plots. These figures illustrate that this profile behavior is consistent for dwarfs orbiting both Andromeda and the Milky Way, regardless of whether they are classified as "ultrafaint" or "dwarf spheroidal". The extension of these NFW-like stellar halos can be traced in some dwarfs to over 2 kpcs in radius. In contrast, the cores are typically 0.5 kpc for dSphs and an order of magnitude smaller on average for UFDs, at 0.05 kpc.
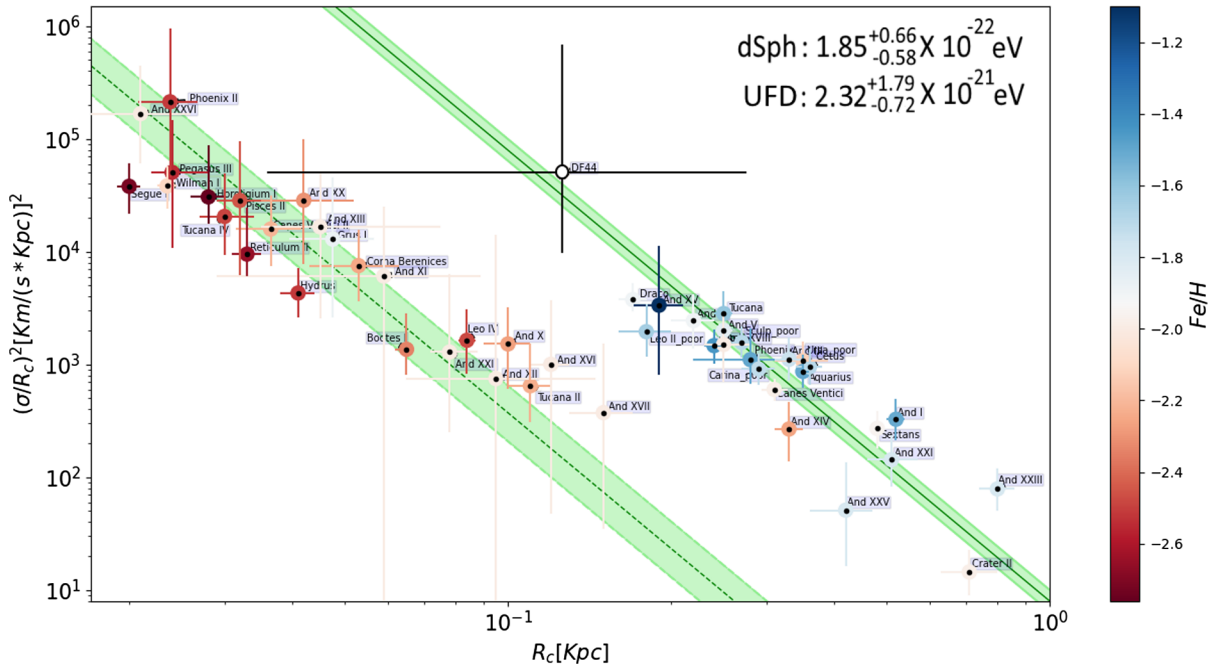

FIG. 5.   DM density vs core radius: Expanding upon the left panel of Fig. 1, we now incorporate color to represent metallicity. It is noteworthy that the ultrafaint galaxies consistently exhibit lower metallicity compared to the dSph class, thus reinforcing the empirical distinction between these two classes of dwarf galaxies, which is based on luminosity.
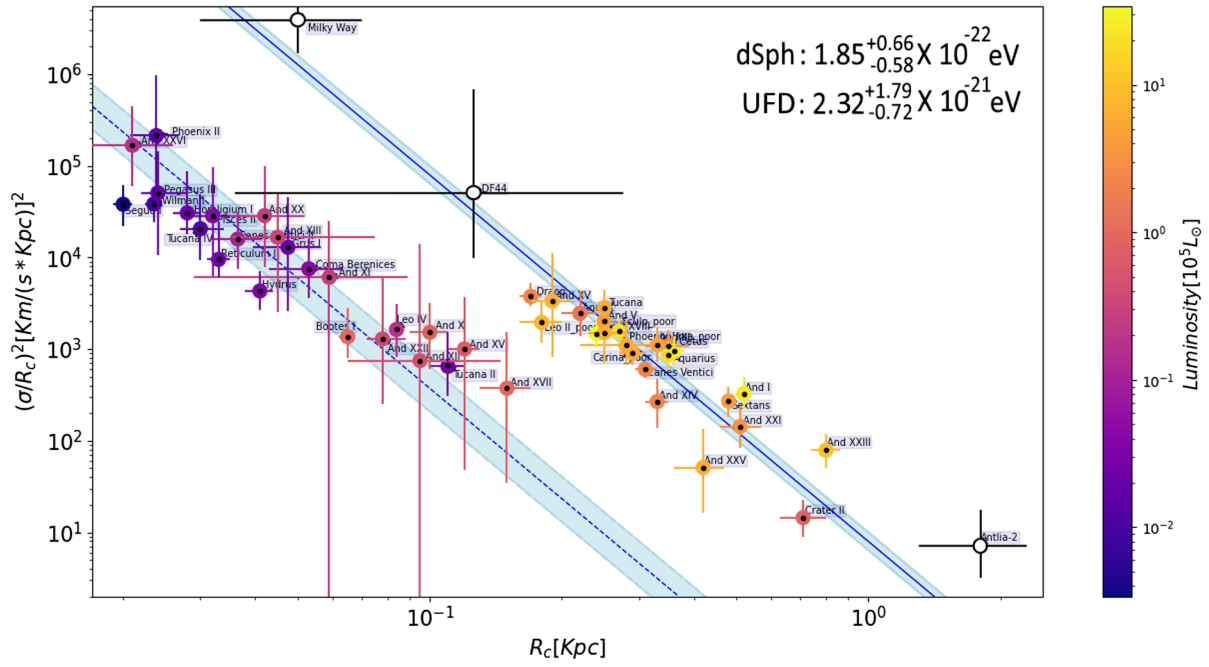
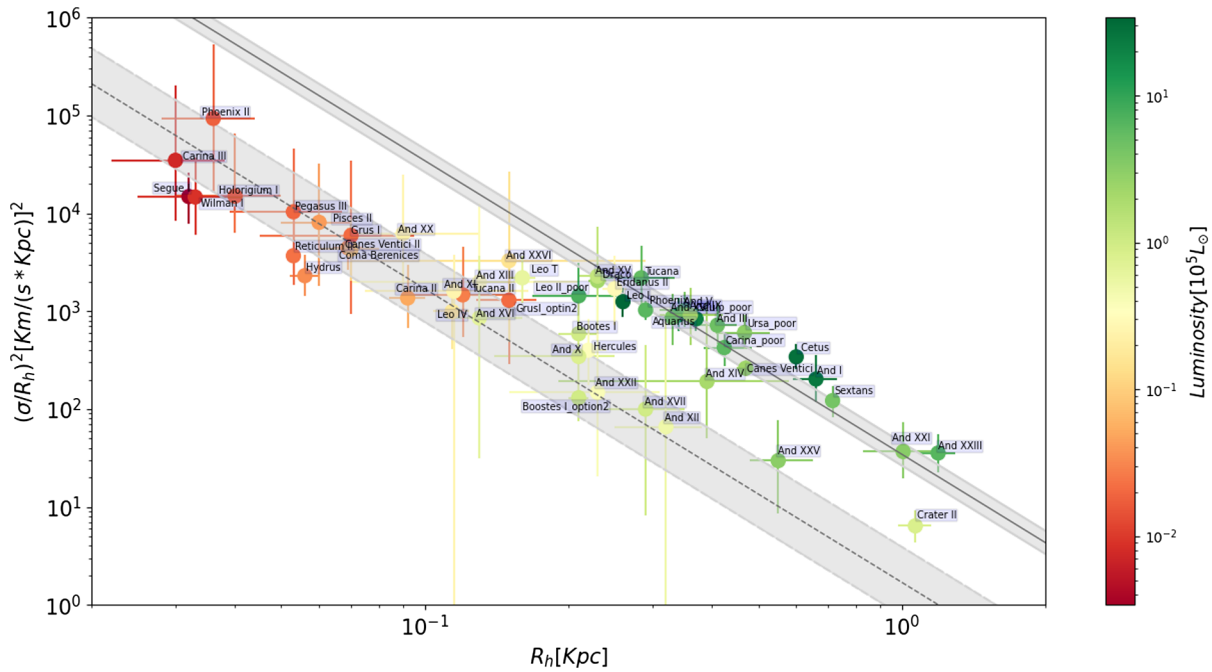FIG. 6.   DM density vs core radius: Expansion of the right panel of Fig. 1.

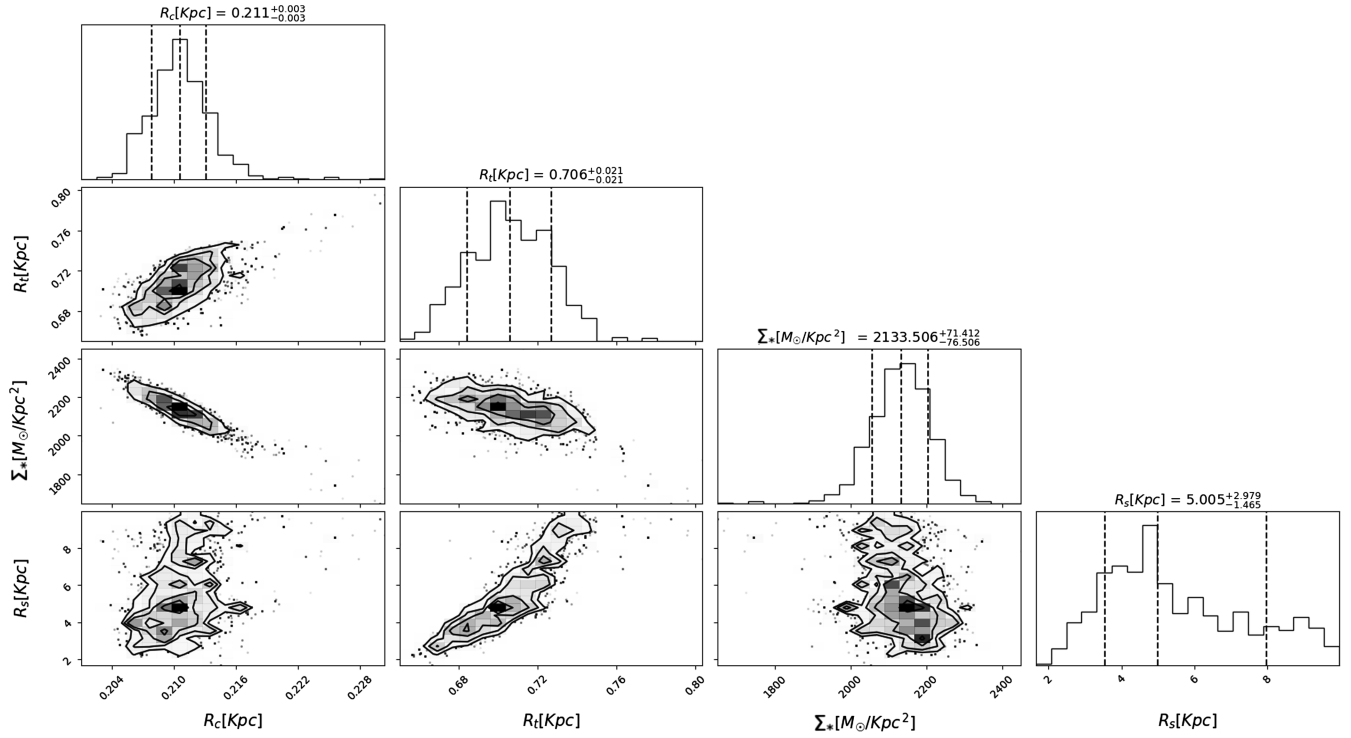FIG. 7.   DM density vs half-light radius: Expansion of the left panel of Fig. 1.

FIG. 8.   All dSph: Classical dwarfs mean profile (Fig. 2 top panel): correlated distributions of the free parameters. As can be seen the core radius and transition radius are well-defined despite wide Gaussian priors, indicating a reliable result. The contours represent the 68%, 95%, and 99% confidence levels. The best-fit parameter values are the medians (with errors), represented by the dashed black ones, and tabulated in Table I.
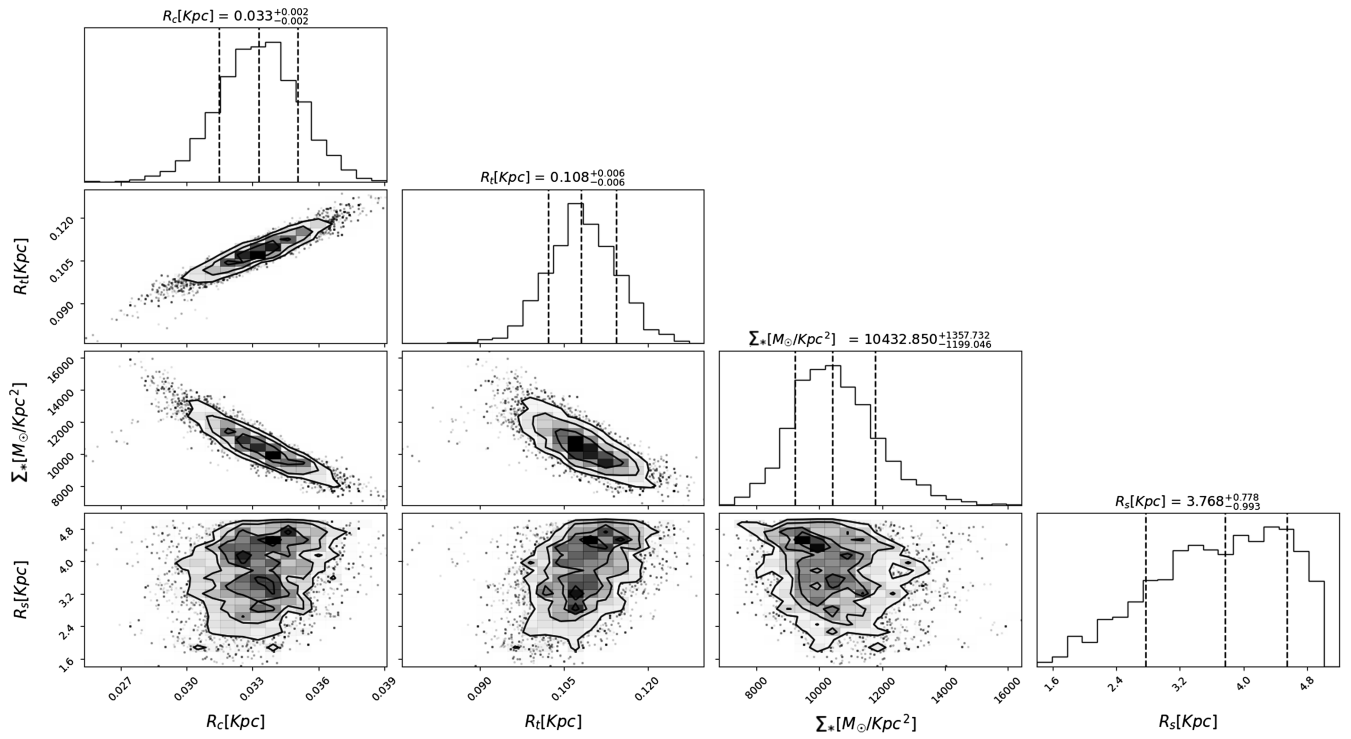
FIG. 9.   All UFD: Ultrafaint dwarfs mean profiles (Fig. 2 lower panel): correlated distributions of the free parameters. As can be seen the core radius and transition radius are well-defined despite wide Gaussian priors, indicating a reliable result. The contours represent the 68%, 95%, and 99% confidence levels. The best-fit parameter values are the medians (with errors), represented by the dashed black curve, and tabulated in Table I.

1. Classical dwarf galaxies

Analysis of the core-halo structure is conducted for all dSph stellar densities. Our predictions for the dSph class $(1.5 \times 10^{-22}$ eV) in ψDM are illustrated in green, representing the 2σ range of the posterior distribution of profiles. We have included nearly all the dSphs within the local group, incorporating stellar profile data points beyond 1.5 kpc. It is crucial to emphasize that all these galaxies are consistent with the core-halo structure, both in the Milky Way and Andromeda, underscoring the universality of this structural pattern for dwarf galaxies.
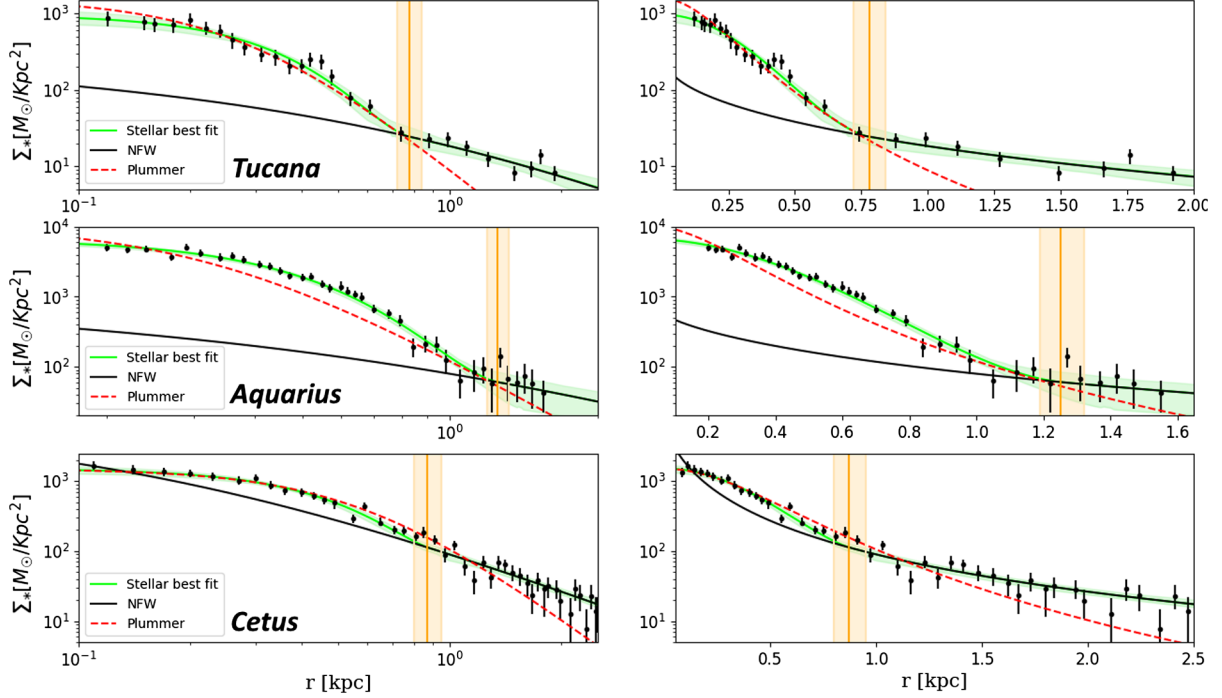
FIG. 10.   Dwarf spheroidal galaxies: This figure presents star count profiles versus dwarf galaxy radius for well-studied dSph dwarf galaxies in the local group, as listed in Table II. In most cases, an extended halo of stars is observable, stretching to approximately ≃2 kpc, most prominently visible on the linear scale of the left-hand panel. Prominent cores are also evident on a scale of less than 1 kpc in each dwarf. A standard Plummer profile (red dashed curve) roughly fits the core region but falls significantly short at larger radii. Our predictions for the dSph class $(\simeq 10^{-22}$ eV) in ψDM are depicted in green, where the distinctive soliton profile provides an excellent fit to the observed cores and the surrounding halo of excited states that azimuthally average to an approximately NFW-like profile beyond the soliton radius. The accuracy of the core fit to the soliton is best observed on a log scale in the right panels, while the left panel in linear scale shows the extent of the halo. This includes the characteristic density drop of about a factor of ≃30 predicted by ψDM between the prominent core and tenuous halo at a radius of approximately 1 kpc, indicated by the vertical orange band. The best-fit MCMC profile parameters are tabulated in the Appendix B, and references to the data in this figure are as follows: Tucana [51], Cetus [52], and Aquarius [53].
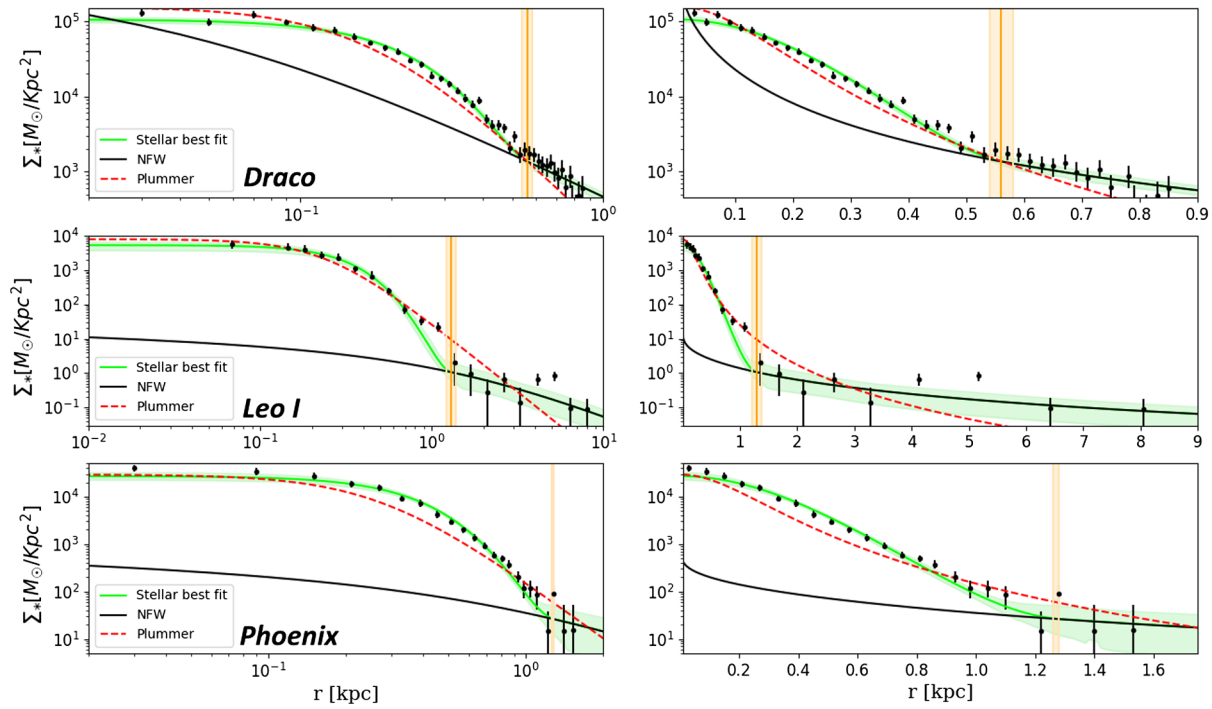
FIG. 11.   Dwarf spheroidal galaxies: Similar to Fig. 10, this figure includes three additional dSph galaxies. References to the data for these galaxies are as follows: Draco [54], Leo I [55], and Phoenix [56].
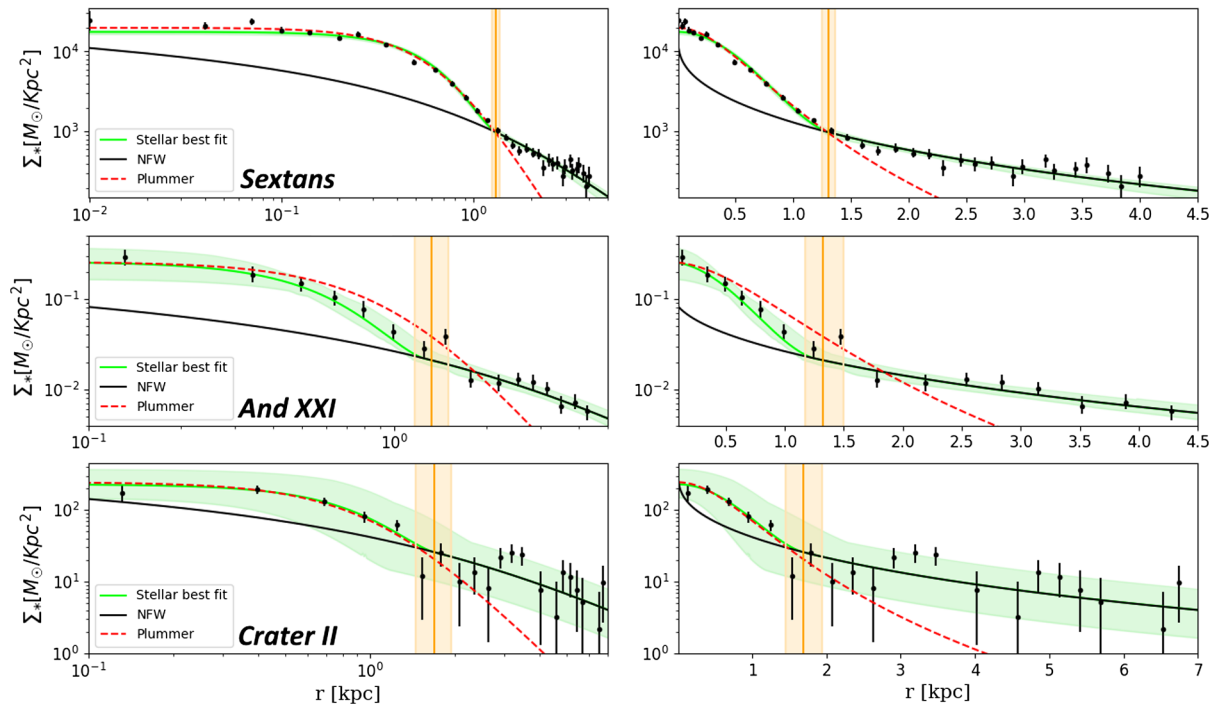

FIG. 12.   Dwarf spheroidal galaxies: In line with Fig. 10, this figure features three additional dSph galaxies. References for the data are as follows: Sextans [57], Andromeda XXI [27], and Crater II [58]. It is noteworthy to highlight that Andromeda XXI exhibits the same ψDM core-halo structure as the dSph satellites of the Milky Way, further supporting the "universality" of this profile for dwarfs.
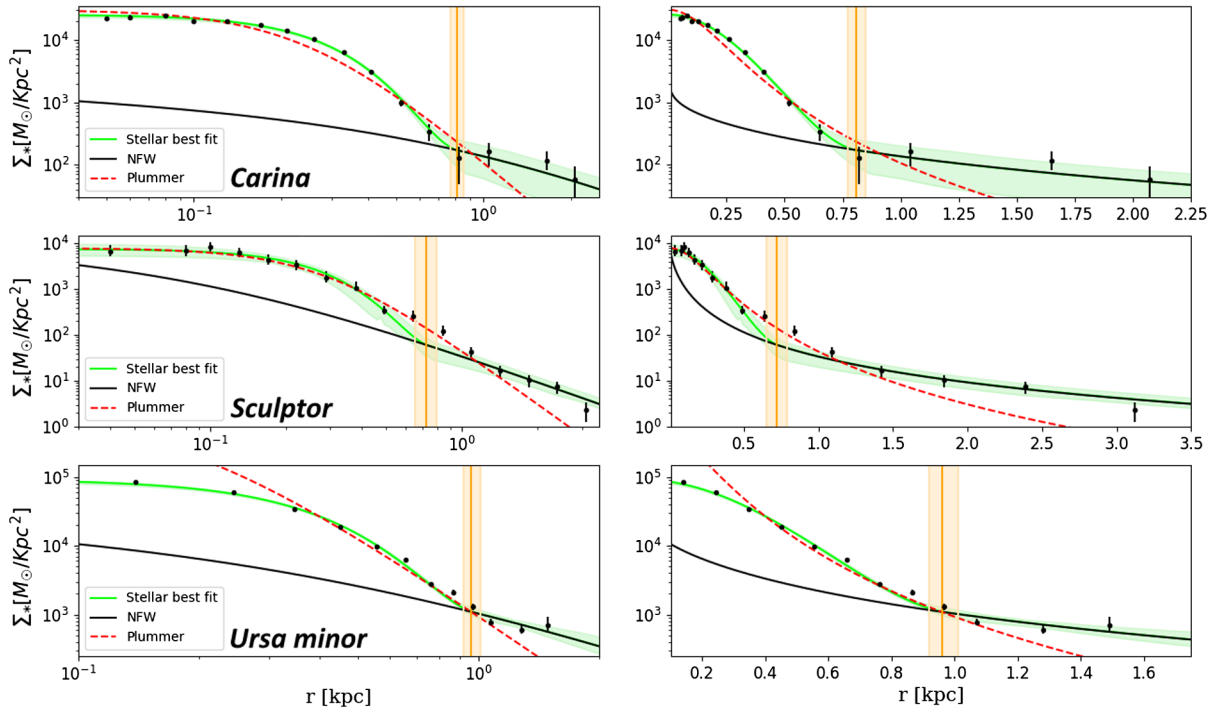
FIG. 13. Dwarf spheroidal galaxies: As in Fig. 10, this figure includes three additional galaxies. References for the data are as follows: Carina [59], Sculptor [59], and Ursa Minor [60].
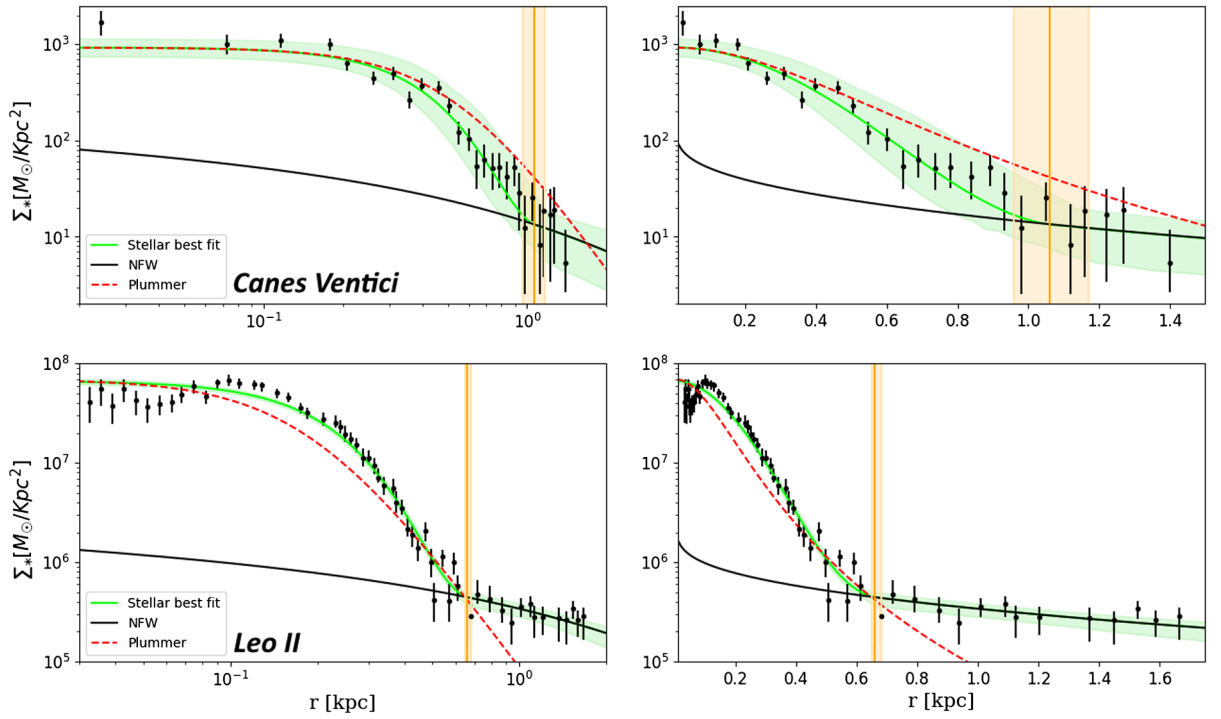

FIG. 14. Dwarf spheroidal galaxies: Similar to Fig. 10, this figure showcases three additional galaxies. References for the data are Canes Venatici [61] and Leo II [62].
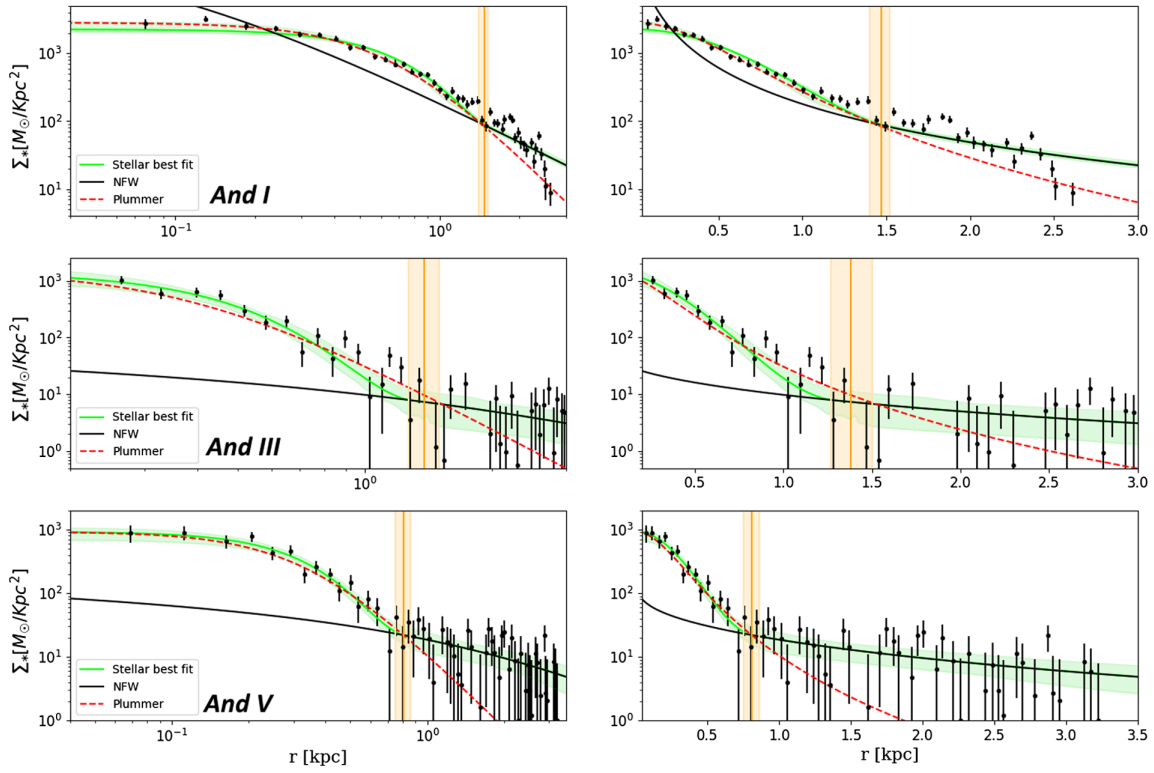
FIG. 15.   Dwarf spheroidal galaxies: Similar to Fig. 10, this figure includes three additional galaxies. Notably, these Andromeda galaxies exhibit the same ψDM core-halo structure as UFD galaxies in the Milky Way, underscoring the universality of the ψDM profile for dwarfs. References for the data are as follows: Andromeda I [63], Andromeda III [64], and Andromeda V [64].
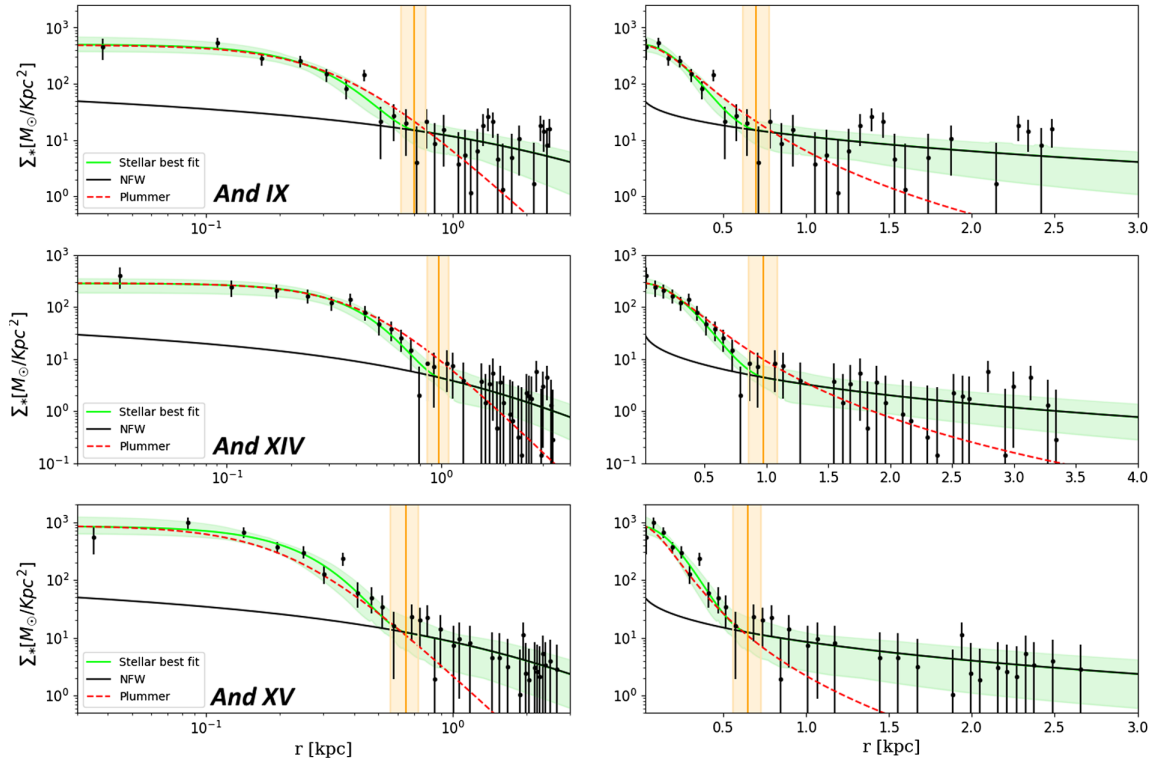

FIG. 16.   Dwarf spheroidal galaxies: As in Fig. 10, this figure includes three additional galaxies. References for the data are Andromeda IX [64], Andromeda XIV [64], and Andromeda XV [64].
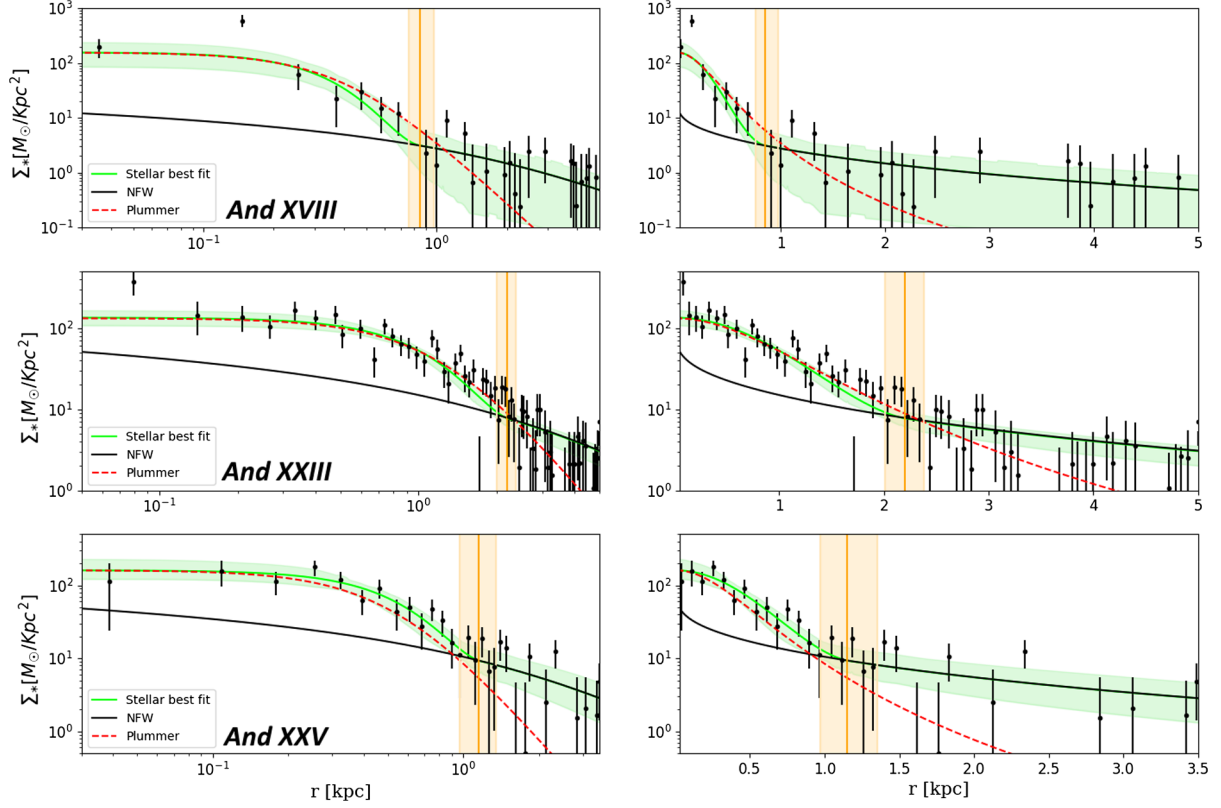
FIG. 17. Dwarf spheroidal galaxies: Similar to Fig. 10, this figure includes three additional galaxies. References for the data are Andromeda XVIII [64], Andromeda XXIII [64], and Andromeda XXV [64].

TABLE II. Observations and ψDM profile fits for dwarf spheroidal galaxies. Column 1: Dwarf galaxy name, Column 2: Core radius r_c, Column 3: Transition point r_t, Column 4: Stellar scale radius r_{s*}, Column 5: Observable projected velocity dispersion $\sigma_{\text{los,obs}}$, Column 6: Observable half-light radius $r_{\text{half,obs}}$, Column 7: Observable luminosity L_{obs}, Column 8: Observable metallicity. We have excluded centrally younger and more metal-rich stellar populations found in some of these dwarfs, which may be attributed to later gas infall. Instead, we adopted the metal-poor stellar and velocity dispersion profiles of Leo II, Carina, Ursa Minor, and Sculptor, with mean velocity dispersion values as follows: $7.96^{+1.39}_{-1.1}$ [65], $8.75^{+0.75}_{-0.75}$ [66,67], $11.5^{+0.9}_{-0.8}$ [68] and $10.7^{+1.4}_{-1.2}$ [32].

Galaxy	r_c (kpc)	r_t (kpc)	r_{s*} (kpc)	$\sigma_{\text{los,obs}}$ (km/s)	$r_{\text{half,obs}}$ (kpc)	L_{obs} ($10^5 L_\odot$)	[Fe/H], obs
Tucana	$0.25^{+0.01}_{-0.01}$	$0.78^{+0.06}_{-0.06}$	$1.05^{+0.50}_{-0.57}$	$13.3^{+2.7}_{-2.3}$ [51]	$0.284^{+0.05}_{-0.05}$ [51]	5.5 [51]	~ -1.6 [69]
Cetus	$0.36^{+0.02}_{-0.02}$	$0.87^{+0.08}_{-0.07}$	$0.24^{+0.14}_{-0.06}$	$11.1^{+1.6}_{-1.3}$ [70]	$0.6^{+0.01}_{-0.01}$ [70]	28^{+8}_{-8} [70]	~ -1.7 [70]
Aquarius	$0.35^{+0.01}_{-0.01}$	$1.25^{+0.07}_{-0.06}$	$1.05^{+0.82}_{-0.64}$	$10.3^{+1.6}_{-1.3}$ [71]	$0.34^{+0.01}_{-0.01}$ [71]	17 [72]	~ -1.5 [72]
Draco	$0.17^{+0.01}_{-0.01}$	$0.56^{+0.02}_{-0.02}$	$0.1^{+0.09}_{-0.05}$	$11^{+2.1}_{-1.5}$ [73]	$0.23^{+0.01}_{-0.01}$ [74]	2.2 [75]	~ -1.9 [76]
Leo I	$0.24^{+0.01}_{-0.01}$	$1.30^{+0.08}_{-0.08}$	$1.75^{+0.78}_{-0.96}$	$9.2^{+1.2}_{-1.2}$ [74]	$0.26^{+0.01}_{-0.01}$ [77]	34^{+11}_{-11} [78]	~ -1.45 [74]
Phoenix	$0.28^{+0.05}_{-0.06}$	$1.27^{+0.01}_{-0.01}$	$1.1^{+0.54}_{-0.55}$	$9.3^{+0.7}_{-0.7}$ [74]	$0.29^{+0.01}_{-0.01}$ [74]	6.2 [79]	~ -1.5 [74]
Canes Ventici	$0.308^{+0.019}_{-0.018}$	$1.06^{+0.11}_{-0.10}$	$2.29^{+1.77}_{-1.35}$	$7.6^{+0.4}_{-0.4}$ [74]	$0.47^{+0.02}_{-0.02}$ [74]	2.3 [80]	$-1.98^{+0.01}_{-0.01}$ [74]
Sextans	$0.48^{+0.01}_{-0.01}$	$1.31^{+0.05}_{-0.06}$	$1.61^{+0.51}_{-0.49}$	$7.9^{+1.3}_{-1.3}$ [74]	$0.715^{+0.01}_{-0.01}$ [57]	$4.37^{+1.69}_{-1.69}$ [81]	~ -1.95 [74]
Crater II	$0.71^{+0.09}_{-0.08}$	$1.68^{+0.25}_{-0.23}$	2.6^{+}_{-}	$2.7^{+0.3}_{-0.3}$ [82]	$1.066^{+0.084}_{-0.084}$ [82]	0.83 [82]	$-1.98^{+0.1}_{-0.1}$ [82]
Leo II	$0.17^{+0.01}_{-0.01}$	$0.66^{+0.02}_{-0.01}$	$3.76^{+0.79}_{-1.07}$	$7.4^{+0.4}_{-0.4}$ [77]	$0.191^{+0.02}_{-0.02}$ [62]	7.4^{+2}_{-2} [83]	~ -1.65 [74]
Carina	$0.21^{+0.01}_{-0.01}$	$0.81^{+0.04}_{-0.04}$	$1.17^{+0.51}_{-0.61}$	$6.6^{+1.2}_{-1.2}$ [74]	$0.424^{+0.06}_{-0.04}$ [84]	5.9 [85]	$-1.72^{+0.01}_{-0.01}$ [74]
Ursa Minor	$0.28^{+0.01}_{-0.01}$	$0.96^{+0.05}_{-0.04}$	$0.52^{+0.9}_{-0.4}$	$11.5^{+0.9}_{-0.8}$ [68]	$0.4675^{+0.06}_{-0.06}$ [68]	3 [86]	~ -2.13 [74]
Sculptor	$0.21^{+0.01}_{-0.01}$	$0.72^{+0.07}_{-0.07}$	$0.12^{+0.25}_{-0.09}$	$10.1^{+0.3}_{-0.3}$ [77]	$0.289^{+0.01}_{-0.01}$ [77]	$20.3^{+7.9}_{-7.9}$ [87]	~ -1.45 [74]
And I	$0.52^{+0.02}_{-0.02}$	$1.47^{+0.05}_{-0.07}$	$0.13^{+0.05}_{-0.02}$	$9.4^{+1.7}_{-1.5}$ [88]	$0.66^{+0.07}_{-0.07}$ [89]	$23.98^{+0.57}_{-0.54}$ [64]	$-1.51^{+0.02}_{-0.02}$ [88]

(Table continued)

TABLE II. *(Continued)*

Galaxy	r_c (kpc)	r_t (kpc)	r_{s*} (kpc)	$\sigma_{los,obs}$ (km/s)	$r_{half,obs}$ (kpc)	L_{obs} ($10^5 L_\odot$)	[Fe/H], obs
And III	$0.33^{+0.02}_{-0.02}$	$1.38^{+0.12}_{-0.11}$	$2.53^{+1.56}_{-0.89}$	$11.0^{+1.9}_{-1.6}$ [88]	$0.41^{+0.04}_{-0.04}$ [64]	$4.78^{+0.11}_{-0.11}$ [64]	$-1.75^{+0.01}_{-0.01}$ [88]
And V	$0.25^{+0.01}_{-0.01}$	$0.81^{+0.05}_{-0.06}$	$2.59^{+1.47}_{-1.37}$	$11.2^{+1.1}_{-1.0}$ [88]	$0.35^{+0.04}_{-0.04}$ [64]	$4.07^{+0.10}_{-0.09}$ [64]	$-1.84^{+0.03}_{-0.03}$ [88]
And IX	$0.22^{+0.02}_{-0.02}$	$0.70^{+0.08}_{-0.08}$	$3.22^{+1.15}_{-1.46}$	$10.9^{+2.0}_{-2.0}$ [90]	$0.36^{+0.06}_{-0.05}$ [64]	$1.99^{+0.52}_{-0.41}$ [90]	$-1.90^{+0.60}_{-0.60}$ [89]
And XIV	$0.33^{+0.02}_{-0.02}$	$0.98^{+0.11}_{-0.12}$	$1.77^{+1.83}_{-1.10}$	$5.4^{+1.3}_{-1.3}$ [91]	$0.39^{+0.19}_{-0.20}$ [89]	$1.99^{+0.52}_{-0.41}$ [90]	$\sim$ []
And XV	$0.19^{+0.02}_{-0.02}$	$0.65^{+0.08}_{-0.09}$	$1.88^{+1.81}_{-1.24}$	$11.0^{+7.0}_{-5.0}$ [92]	$0.23^{+0.03}_{-0.02}$ [89]	$1.25^{+0.74}_{-0.25}$ [90]	~ -1.1 [89]
And XVIII	$0.25^{+0.03}_{-0.02}$	$0.85^{+0.12}_{-0.09}$	$2.99^{+1.27}_{-1.49}$	$9.7^{+2.3}_{-2.3}$ [93]	$0.33^{+0.02}_{-0.02}$ [89]	$3.98^{+2.32}_{-1.47}$ [93]	$-1.80^{+0.50}_{-0.50}$ [89]
And XXI	$0.51^{+0.06}_{-0.05}$	$1.32^{+0.18}_{-0.15}$	$3.16^\pm$	$6.1^{+1}_{-0.9}$ [27]	$1.005^{+0.175}_{-0.175}$ [27]	$3.2^{+0.8}_{-0.7}$ [27]	~ -1.8 [27]
And XXIII	$0.80^{+0.06}_{-0.06}$	$2.20^{+0.18}_{-0.19}$	$3.92^{+0.70}_{-1.35}$	$7.1^{+1.0}_{-1.0}$ [90]	$1.19^{+0.10}_{-0.10}$ [89]	$6.30^{+1.64}_{-1.29}$ [90]	$-1.80^{+0.20}_{-0.20}$ [89]
And XXV	$0.42^{+0.05}_{-0.06}$	$1.15^{+0.20}_{-0.18}$	$2.79^{+1.30}_{-1.18}$	$3.0^{+1.2}_{-1.1}$ [90]	$0.55^{+0.10}_{-0.07}$ [64]	$3.16^{+0.82}_{-0.65}$ [90]	$-1.80^{+0.50}_{-0.50}$ [89]

2. Ultrafaint dwarf galaxies

Analysis of the core-halo structure has been conducted for all UFD stellar densities. Our predictions for the UFD class $(1.5 \times 10^{-21}$ eV) in ψDM are illustrated in green, representing the 2σ range of the posterior distribution of profiles. We have included nearly all the UFDs within the local group, incorporating stellar profile data points beyond 0.25 kpc. It is crucial to emphasize that all these galaxies are consistent with the core-halo structure, both in the Milky Way and Andromeda, underscoring the universality of this structural pattern for dwarf galaxies.
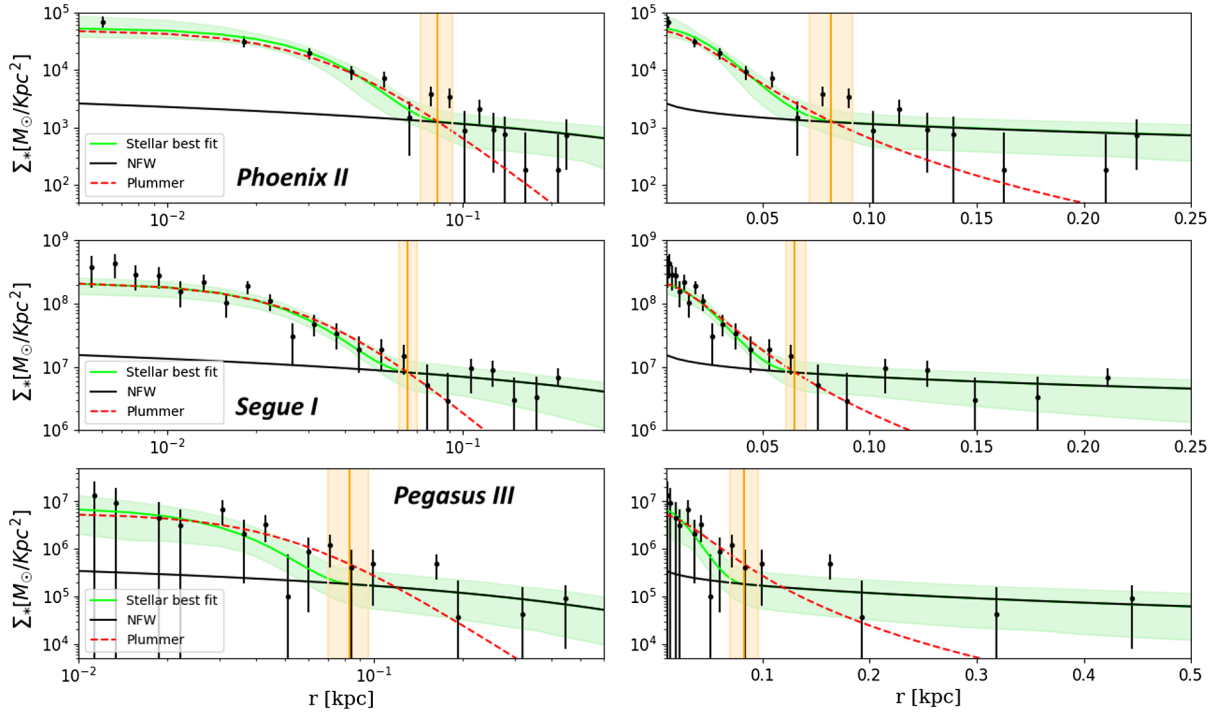

FIG. 18.   Ultrafaint dwarfs: This figure presents the star count profiles versus dwarf galaxy radius for the "ultrafaint" dwarf galaxies in the local group, as listed in Table III. Many UFD dwarfs show clear evidence of extended halos stretching to approximately $\simeq 0.5$ kpc, most notably visible on the linear scale of the left-hand panel. Cores are also apparent on a scale of less than 0.1 kpc in these UFD dwarfs. A standard Plummer profile (red dashed curve) is observed to roughly fit the core region but falls significantly short at large radius. The soliton profile, normalized to the mean boson mass estimated for these dwarfs ($\simeq 10^{-21}$ eV), is shown in green. The distinctive soliton profile provides an excellent fit to the observed cores, surrounded by a halo of excited states that azimuthally average to an approximately NFW-like profile beyond the soliton radius. The cores align well with the predicted form of the soliton profile, as best seen on a log scale in the right panels. The best-fit MCMC profile parameters are tabulated in the Appendix B. References for the data are as follows: Phoenix II [94], Segue I [62], and Pegasus III [62].
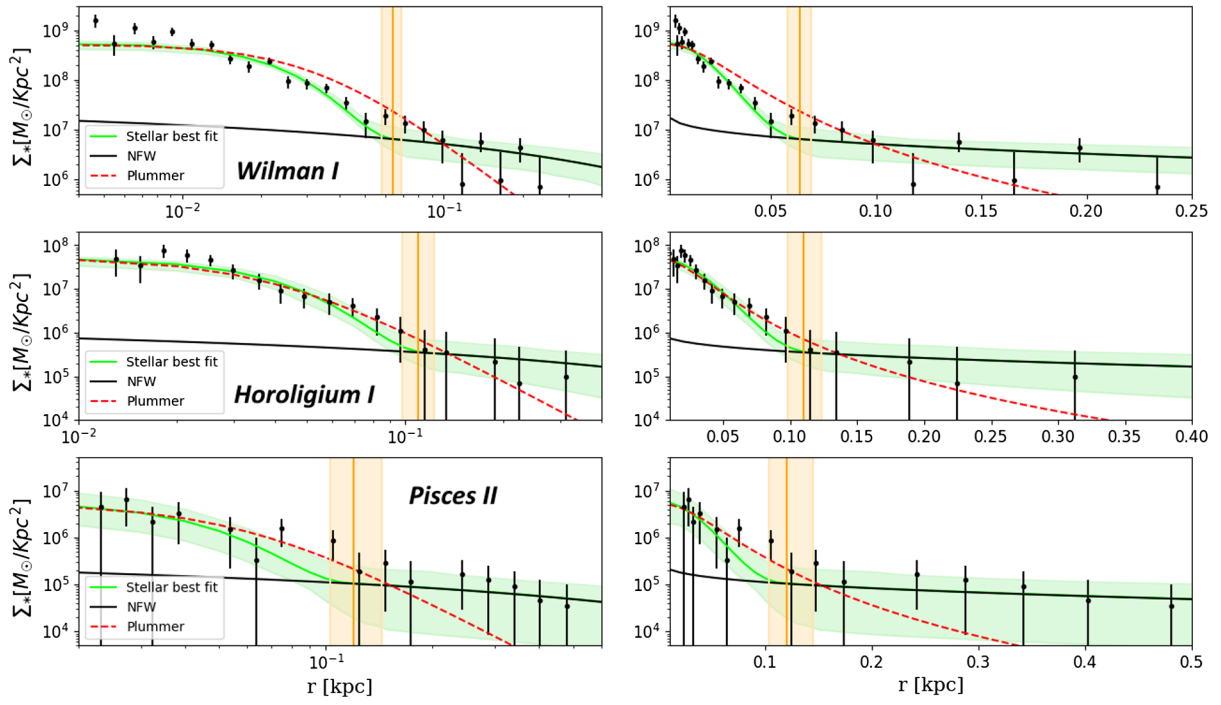
FIG. 19.   Ultrafaint dwarf galaxies: Similar to Fig. 15, this figure includes three additional galaxies. References for the data are as follows: Wilman I [62], Horologium I [62], and Pisces II [62].
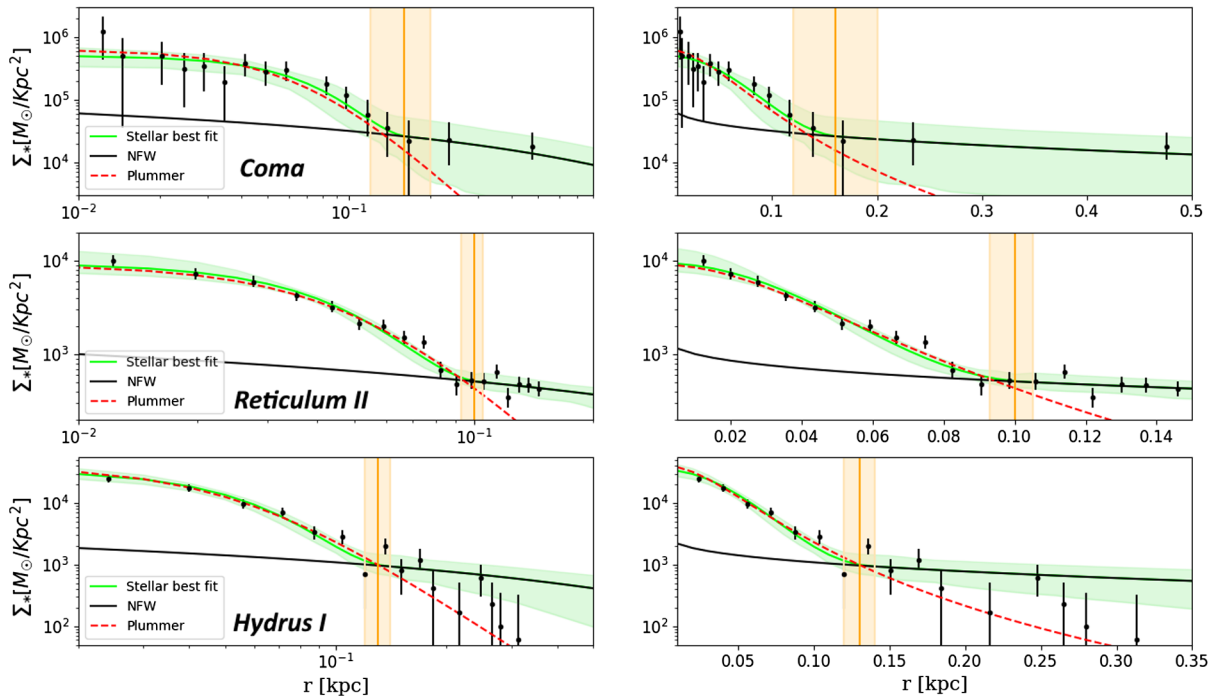

FIG. 20.   Ultrafaint dwarf galaxies: Similar to Fig. 15, this figure includes three additional galaxies. References for the data are as follows: Coma Berenices [62], Reticulum II [95], and Hydrus I [96].
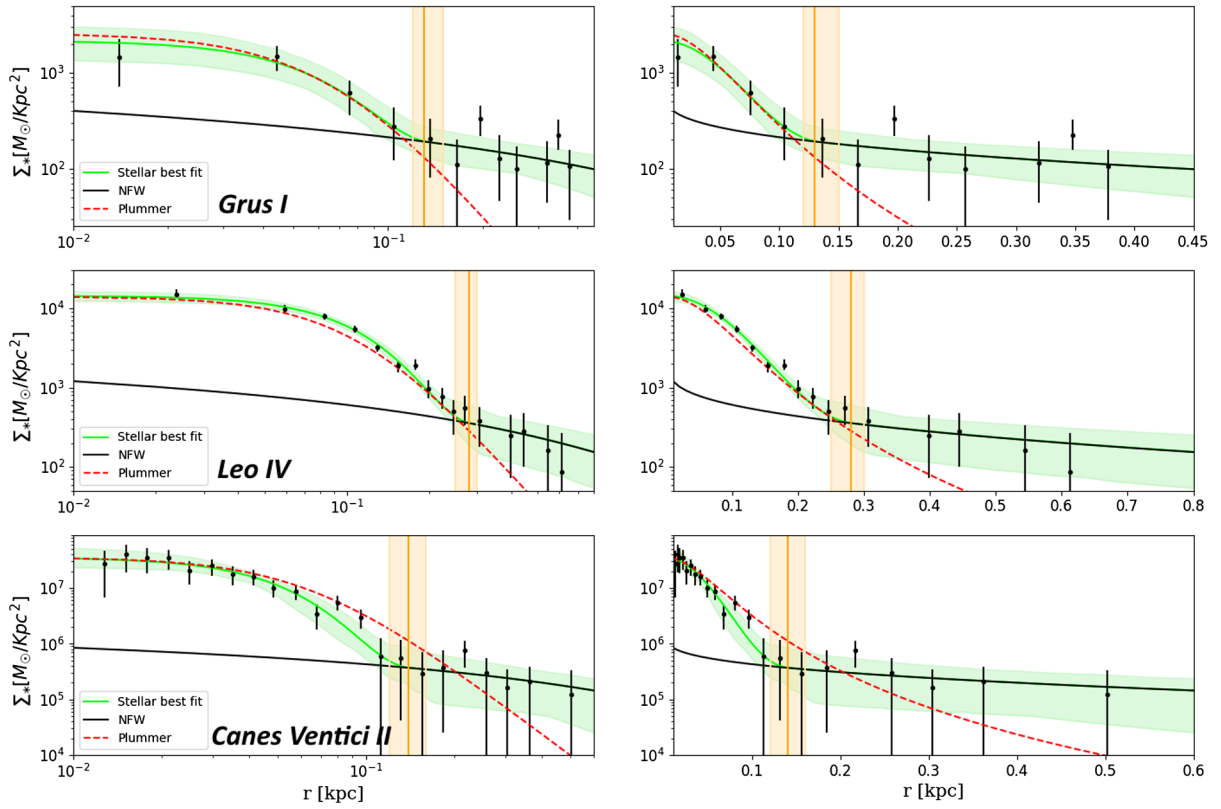
FIG. 21.   Ultrafaint dwarf galaxies: Similar to Fig. 15, this figure includes three additional galaxies. References for the data are as follows: Grus I [96], Leo IV [97], and Canes Venatici II [96].
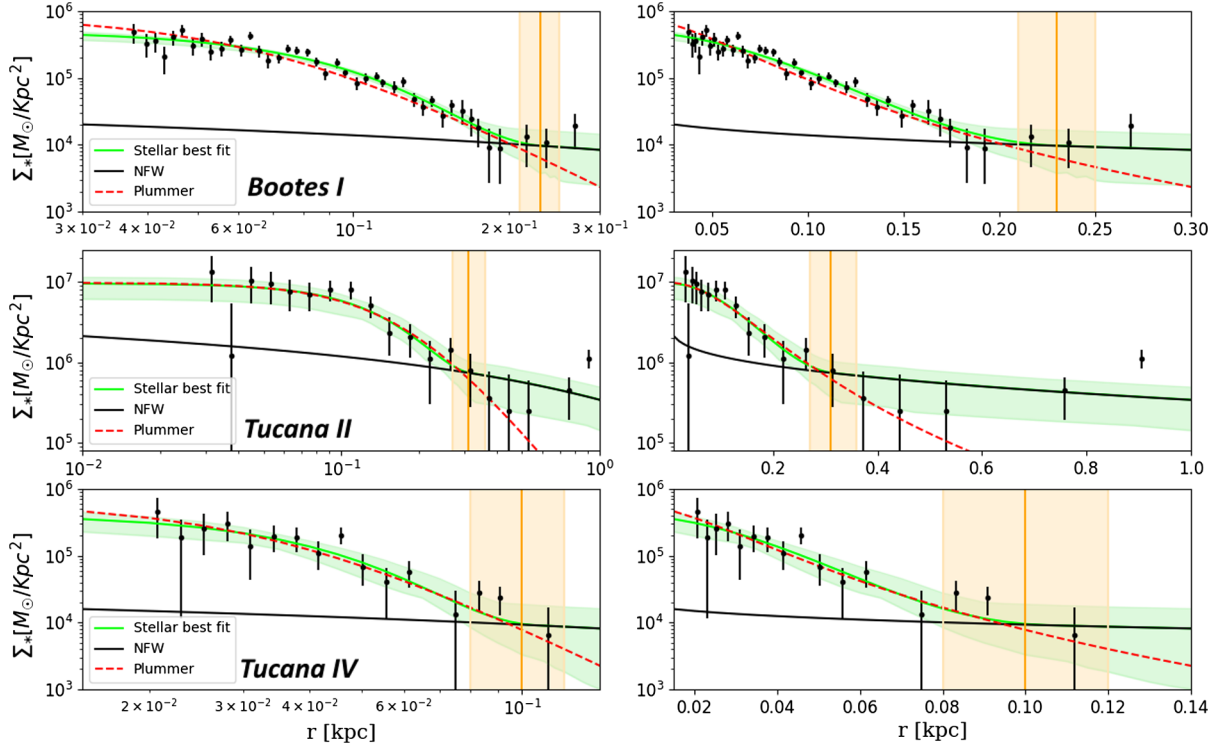

FIG. 22.   Ultrafaint dwarf galaxies: Similar to Fig. 15, this figure includes three additional galaxies. References for the data are as follows: Bootes I [62], Tucana II [98], and Tucana IV [62]. It's worth noting that Chiti *et al.* [26] claimed a surprisingly extended halo of stars and dark matter, extending to 1 kpc in extent for Tucana II.
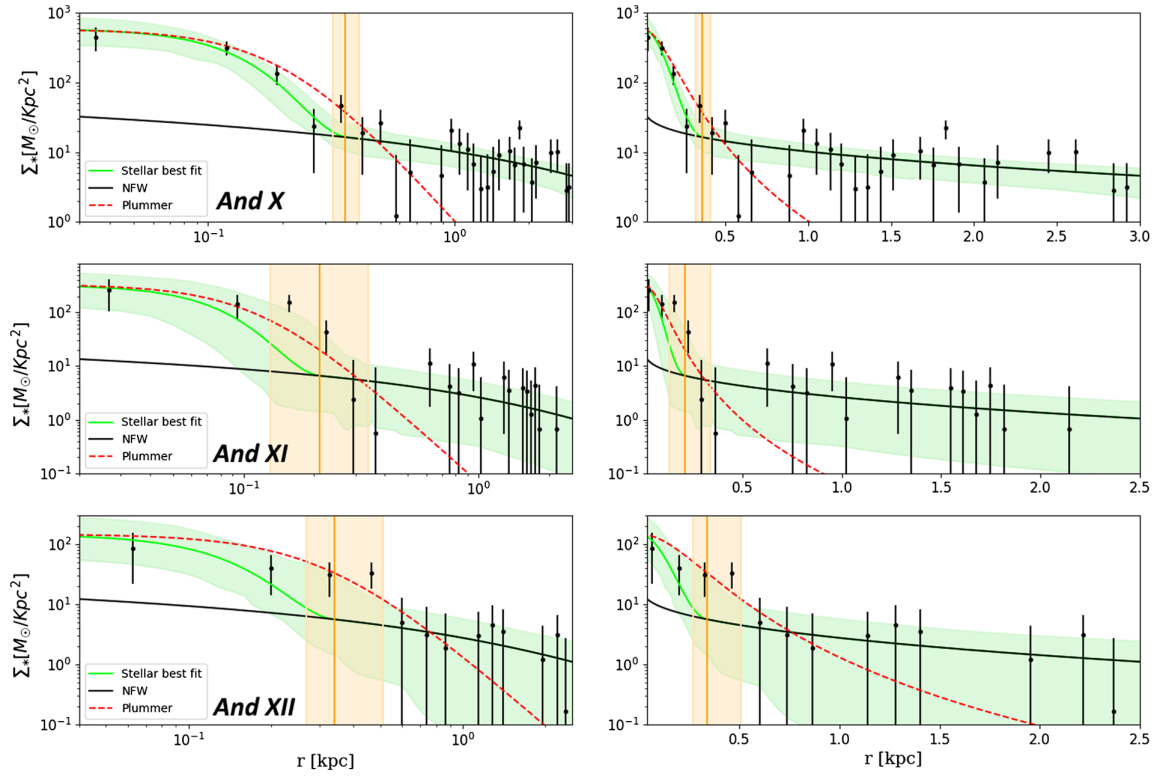
FIG. 23. Ultrafaint dwarf galaxies: Similar to Fig. 15, this figure includes three additional galaxies. References for the data are as follows: Andromeda X [64], Andromeda XI [64], and Andromeda XII [64].
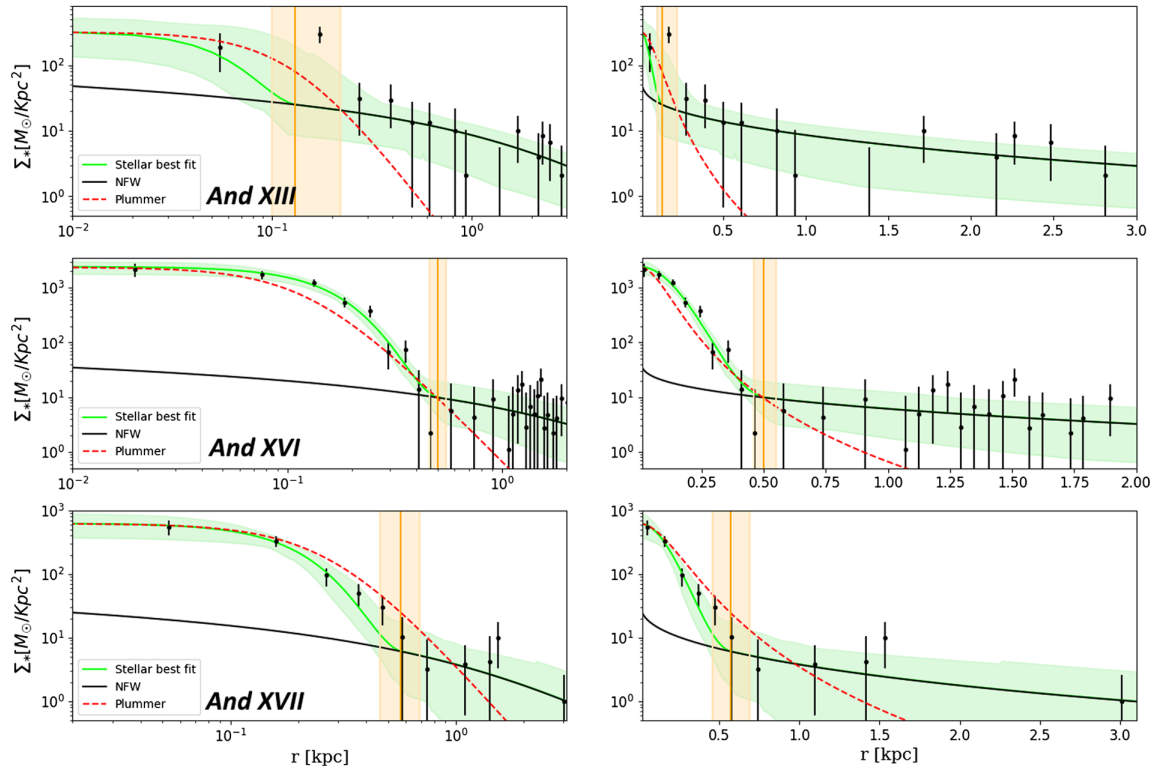

FIG. 24. Ultrafaint dwarf galaxies: Similar to Fig. 15, this figure includes three additional galaxies. References for the data are as follows: Andromeda XIII [64], Andromeda XVI [64], and Andromeda XVII [99].
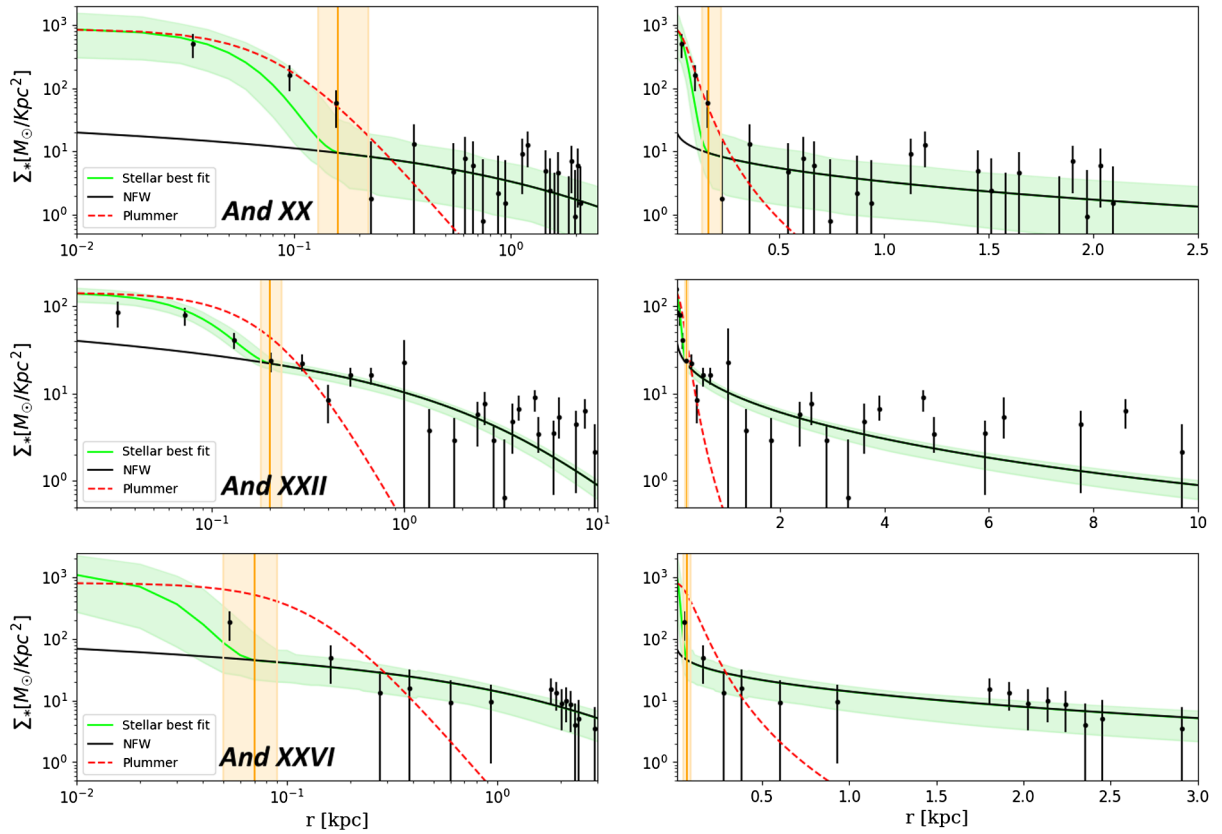
FIG. 25. Ultrafaint dwarf galaxies: Similar to Fig. 15, this figure includes three additional galaxies. References for the data are as follows: Andromeda XX [64], Andromeda XXII [100], and Andromeda XXVI [64].

TABLE III. Observations and ψDM profile fits to ultrafaint dwarf galaxies. Column 1: UFD name, Column 2: Core radius r_c, Column 3: Transition point r_t, Column 4: Stellar scale radius r_{s*}, Column 5: Observable projected velocity dispersion $\sigma_{\rm los,obs}$, Column 6: Observable half-light radius $r_{\rm half,obs}$, Column 7: Observable luminosity $L_{\rm obs}$, Column 8: Observable age, Column 9: Observable metallicity. Note: Leo V has recently been suggested not to be a galaxy.

Galaxy	r_c (kpc)	r_t (kpc)	r_{s*} (kpc)	$\sigma_{\rm los}$ (km/s)	$r_{\rm half,obs}$ (kpc)	L, obs ($10^3 L_\odot$)	[Fe/H], obs
Phoenix II	$0.024^{+0.003}_{-0.003}$	$0.082^{+0.01}_{-0.01}$	$1.37^{+1.17}_{-1.10}$	$11^{+9.40}_{-5.3}$ [77]	$0.036^{+0.008}_{-0.008}$ [77]	$1.79^{+1.41}_{-0.79}$ [101]	$-2.51^{+0.19}_{-0.17}$ [77]
Segue I	$0.020^{+0.001}_{-0.001}$	$0.065^{+0.005}_{-0.004}$	$1.59^{+0.81}_{-0.77}$	$3.9^{+0.8}_{-0.8}$ [74]	$0.032^{+0.003}_{-0.003}$ [74]	$0.28^{+0.27}_{-0.14}$ [101]	$-2.72^{+0.4}_{-0.4}$ [74]
Pegasus III	$0.024^{+0.004}_{-0.002}$	$0.083^{+0.013}_{-0.013}$	$1.16^{+1.10}_{-0.76}$	$5.4^{+3}_{-2.5}$ [77]	$0.053^{+0.014}_{-0.014}$ [77]	1.96 [102]	$-2.55^{+0.15}_{-0.15}$ [77]
Wilman I	$0.0235^{+0.001}_{-0.001}$	$0.064^{+0.005}_{-0.006}$	$0.64^{+1.21}_{-0.44}$	$4^{+0.8}_{-0.8}$ [77]	$0.033^{+0.008}_{-0.008}$ [77]	$0.87^{+0.86}_{-0.43}$ [101]	~ -2.1 [77]
Horoligium I	$0.028^{+0.002}_{-0.002}$	$0.11^{+0.013}_{-0.012}$	$1.29^{+1.01}_{-0.87}$	$4.9^{+2.8}_{-0.9}$ [77]	$0.041^{+0.01}_{-0.01}$ [77]	$2.24^{+1.51}_{-0.90}$ [101]	$-2.76^{+0.10}_{-0.10}$ [77]
Pisces II	$0.032^{+0.006}_{-0.003}$	$0.12^{+0.024}_{-0.017}$	$1.85^{+1.30}_{-1.19}$	$5.4^{+3.6}_{-2.4}$ [77]	$0.062^{+0.01}_{-0.01}$ [77]	$4.16^{+1.76}_{-1.22}$ [101]	$-2.45^{+0.07}_{-0.07}$ [77]
Coma Berenices	$0.053^{+0.010}_{-0.011}$	$0.16^{+0.04}_{-0.04}$	$1.67^{+0.79}_{-0.90}$	$4.6^{+0.8}_{-0.8}$ [77]	$0.069^{+0.005}_{-0.005}$ [77]	$4.81^{+1.24}_{-0.99}$ [101]	$-2.25^{+0.05}_{-0.05}$ [77]
Reticulum II	$0.0333^{+0.002}_{-0.002}$	$0.10^{+0.005}_{-0.007}$	$1.48^{+1.04}_{-0.85}$	$3.22^{+1.64}_{-0.49}$ [74]	$0.053^{+0.002}_{-0.002}$ [74]	$2.36^{+0.2}_{-0.2}$ [103]	$-2.65^{+0.07}_{-0.07}$ [103]
Hydrus	$0.041^{+0.003}_{-0.003}$	$0.13^{+0.01}_{-0.01}$	$1.27^{+1.01}_{-0.87}$	$2.69^{+0.51}_{-0.43}$ [74]	$0.056^{+0.004}_{-0.004}$ [74]	3.38 [96]	$-2.52^{+0.09}_{-0.09}$ [96]
Grus I	$0.0475^{+0.009}_{-0.008}$	$0.13^{+0.02}_{-0.01}$	$1.79^{+0.72}_{-0.76}$	$5.4^{+3}_{-2.5}$ [77]	$0.070^{+0.025}_{-0.025}$ [74]	$2.10^{+1.51}_{-0.88}$ [101]	$-1.88^{+0.09}_{-0.03}$ [77]
Leo IV	$0.084^{+0.003}_{-0.003}$	$0.28^{+0.02}_{-0.03}$	$1.34^{+1.42}_{-0.34}$	$3.4^{+1.3}_{-0.9}$ [104]	$0.114^{+0.01}_{-0.01}$ [104]	18^{+8}_{-8} [105]	$-2.48^{+0.16}_{-0.13}$ [104]
Canes Ventici II	$0.037^{+0.005}_{-0.005}$	$0.14^{+0.02}_{-0.02}$	$1.39^{+0.99}_{-0.93}$	$4.6^{+1.0}_{-1.0}$ [77]	$0.07^{+0.01}_{-0.01}$ [101]	$10.46^{+3.05}_{-3.05}$ [101]	$-2.21^{+0.05}_{-0.05}$ [74]
Bootes I	$0.065^{+0.002}_{-0.003}$	$0.23^{+0.02}_{-0.02}$	$1.86^{+0.73}_{-1.03}$	$2.4^{+0.9}_{-0.5}$ [77]	$0.22^{+0.01}_{-0.01}$ [77]	$21.78^{+5.64}_{-4.48}$ [101]	$-2.34^{+0.05}_{-0.05}$ [104]
Tucana II	$0.11^{+0.01}_{-0.01}$	$0.31^{+0.05}_{-0.04}$	$2.45^{+0.98}_{-1.09}$	$2.8^{+1.2}_{-0.7}$ [98]	$0.12^{+0.03}_{-0.03}$ [98]	~ 2.83 [101]	~ -2.7 [26]

(Table continued)

TABLE III. *(Continued)*

Galaxy	r_c (kpc)	r_t (kpc)	r_{s*} (kpc)	σ_{los} (km/s)	$r_{half,obs}$ (kpc)	L, obs ($10^3 L_\odot$)	[Fe/H], obs
Tucana IV	$0.030^{+0.004}_{-0.003}$	$0.10^{+0.02}_{-0.02}$	$1.90^{+1.31}_{-1.21}$	$4.3^{+1.7}_{-1.0}$ [77]	$0.11^{+0.011}_{-0.009}$ [62]	$1.40^{+0.60}_{-0.30}$ [106]	$-2.49^{+0.15}_{-0.16}$ [77]
Leo V*	$0.021^{+0.002}_{-0.001}$	$0.076^{+0.007}_{-0.007}$	$1.61^{+1.50}_{-1.16}$	$3.7^{+2.3}_{-1.4}$ [74]	$0.055^{+0.02}_{-0.02}$ [77]	$4.92^{+1.93}_{-1.39}$ [101]	$-2.28^{+0.15}_{-0.16}$ [77]
And X	$0.10^{+0.01}_{-0.01}$	$0.36^{+0.05}_{-0.04}$	$6.18^{+2.47}_{-2.87}$	$3.9^{+1.2}_{-1.2}$ [107]	$0.21^{+0.04}_{-0.07}$ [64]	$79.43^{+20.57}_{-16.}$ [64]	$-2.27^{+0.03}_{-0.03}$ [89]
And XI	$0.059^{+0.03}_{-0.02}$	$0.21^{+0.13}_{-0.08}$	$2.67^{+1.43}_{-1.44}$	≤ 4.6 [108]	$0.12^{+0.05}_{-0.04}$ [64]	$25.12^{+14.69}_{-9.28}$ [64]	$-2.0^{+0.20}_{-0.20}$ [89]
And XII	$0.10^{+0.05}_{-0.02}$	$0.34^{+0.17}_{-0.07}$	$2.62^{+1.37}_{-1.33}$	$2.6^{+5.1}_{-2.6}$ [107]	$0.32^{+0.06}_{-0.07}$ [89]	$50.12^{+29.31}_{-18.50}$ [64]	$-2.0^{+0.2}_{-0.2}$ [89]
And XIII	$0.045^{+0.03}_{-0.01}$	$0.13^{+0.09}_{-0.03}$	$2.96^{+1.21}_{-1.28}$	$5.8^{+2.0}_{-2.0}$ [107]	$0.13^{+0.08}_{-0.06}$ [64]	$31.62^{+18.50}_{-15.77}$ [64]	$-2.0^{+0.16}_{-0.13}$ [89]
And XVI	$0.12^{+0.01}_{-0.01}$	$0.50^{+0.05}_{-0.04}$	$2.84^{+1.34}_{-1.57}$	$3.8^{+2.9}_{-2.9}$ [107]	$0.13^{+0.03}_{-0.02}$ [64]	$63.09^{+16.34}_{-12.97}$ [64]	$-2.0^{+0.5}_{-0.5}$ [89]
And XVII	$0.15^{+0.02}_{-0.02}$	$0.57^{+0.12}_{-0.11}$	$1.84^{+1.54}_{-1.25}$	$2.9^{+2.2}_{-1.9}$ [93]	$0.29^{+0.06}_{-0.05}$ [64]	$100.00^{+25.89}_{-20.57}$ [64]	~-2.0 [89]
And XX	$0.042^{+0.01}_{-0.007}$	$0.16^{+0.06}_{-0.03}$	$2.64^{+1.48}_{-1.27}$	$7.1^{+3.9}_{-2.5}$ [93]	$0.09^{+0.04}_{-0.02}$ [64]	$25.12^{+14.69}_{-9.27}$ [64]	$-2.3^{+0.5}_{-0.5}$ [89]
And XXII	$0.078^{+0.01}_{-0.006}$	$0.20^{+0.03}_{-0.02}$	$4.57^{+0.31}_{-0.47}$	$2.8^{+2.9}_{-1.4}$ [93]	$0.23^{+0.08}_{-0.08}$ [64]	$39.81^{+23.29}_{-19.86}$ [64]	$-1.85^{+0.10}_{-0.10}$ [89]
And XXVI	$0.021^{+0.005}_{-0.004}$	$0.07^{+0.02}_{-0.02}$	$3.65^{+0.86}_{-1.19}$	$8.6^{+2.8}_{-2.2}$ [93]	$0.15^{+0.14}_{-0.08}$ [64]	$15.85^{+24.00}_{-9.57}$ [64]	$-1.9^{+0.20}_{-0.20}$ [89]

In this analysis, we examine the satellites of the Milky Way and Andromeda separately to determine if there are any differences in core-halo structure, as depicted in Figs. 26 and 32. Additionally, we explore the density versus core radius trend in Figs. 28 and 34.
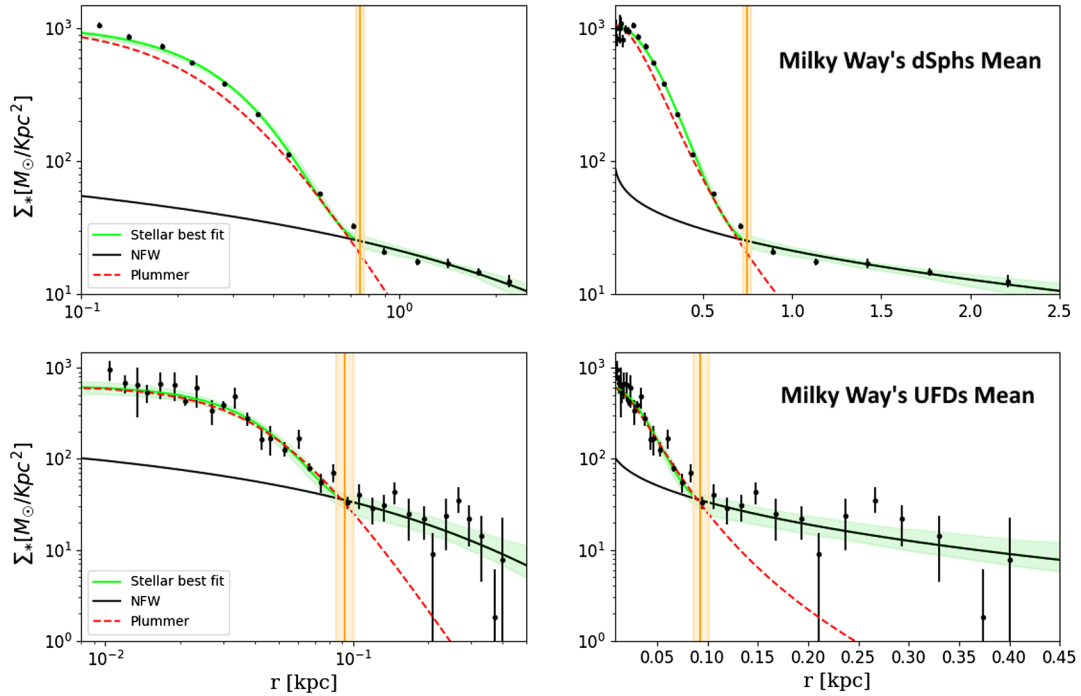
3. Milky Way

Milky Way's galaxies alone.

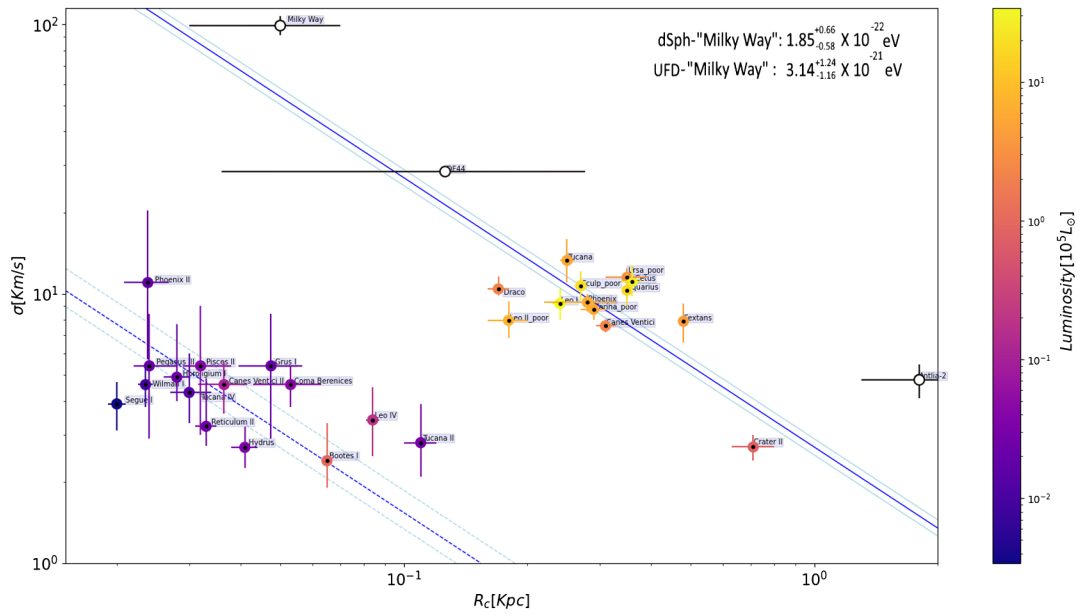
FIG. 26. Like Fig. 2 but just for Milky Way's satellites.

FIG. 27.   Velocity dispersion vs core radius: Like Fig. 3 but just for Milky Way's satellites.
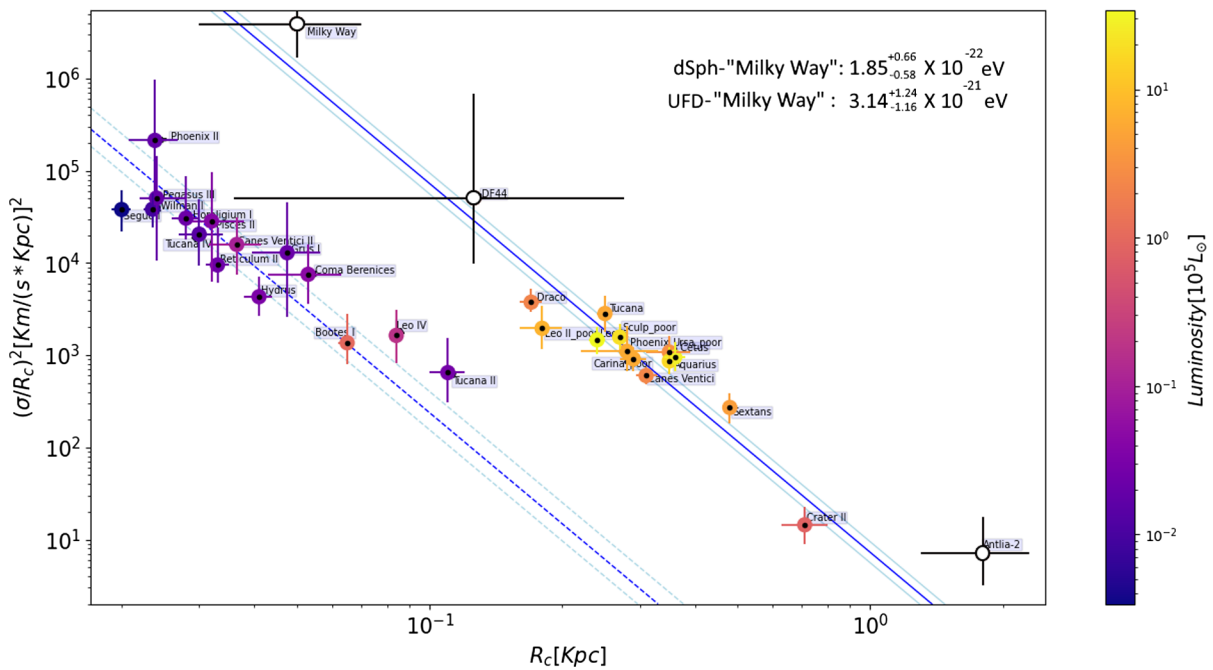

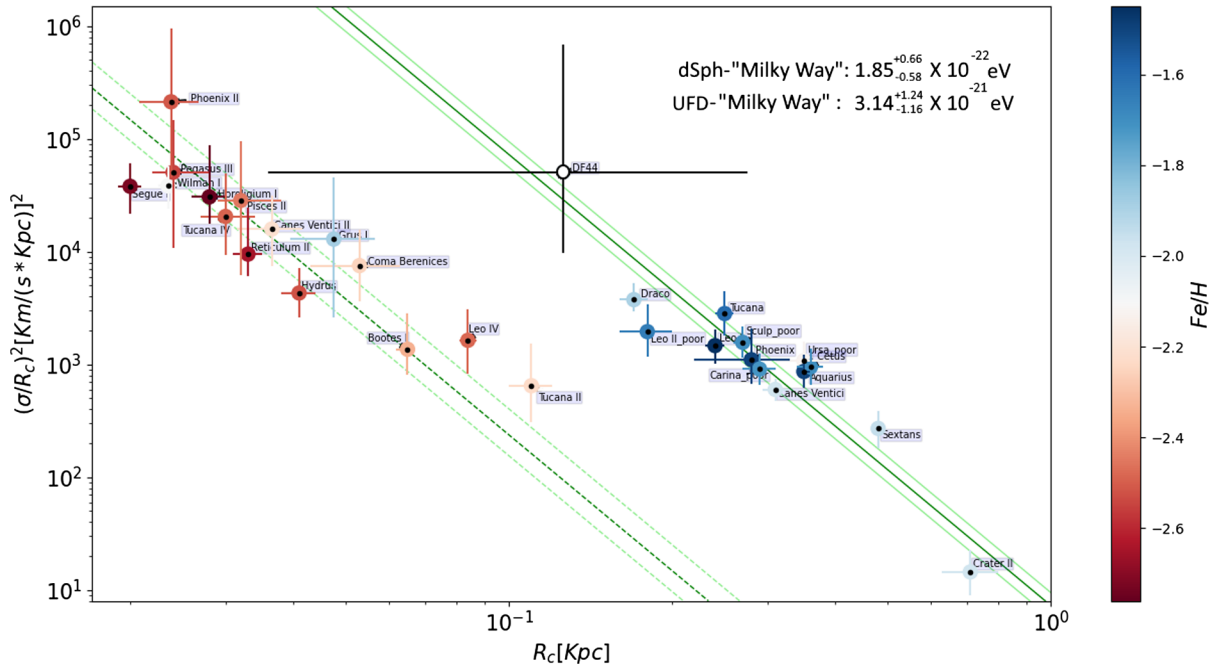FIG. 28.   DM density vs core radius: Like Fig. 1 just for Milky Way's satellites.

FIG. 29.   DM density vs core radius: Like Fig. 5 but just for Milky Way's satellites.
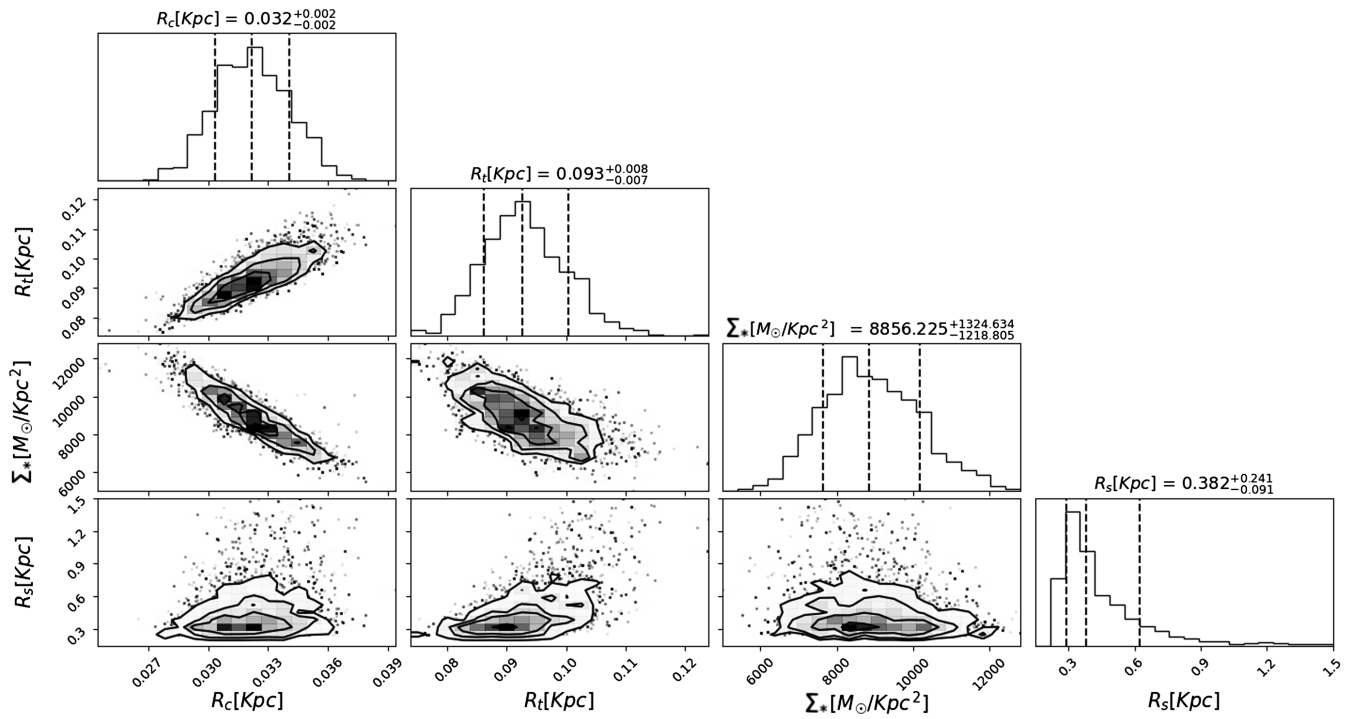

FIG. 30.   Milky Way's UFD mean (Fig. 26 lower panel): Correlated distributions of the free parameters. As can be seen the core radius and transition radius are well-defined despite the wide Gaussian priors, indicating a reliable result. The contours represent the 68%, 95%, and 99% confidence levels. The best-fit parameter values are the medians (with errors), represented by the dashed black ones, and tabulated in Table I.
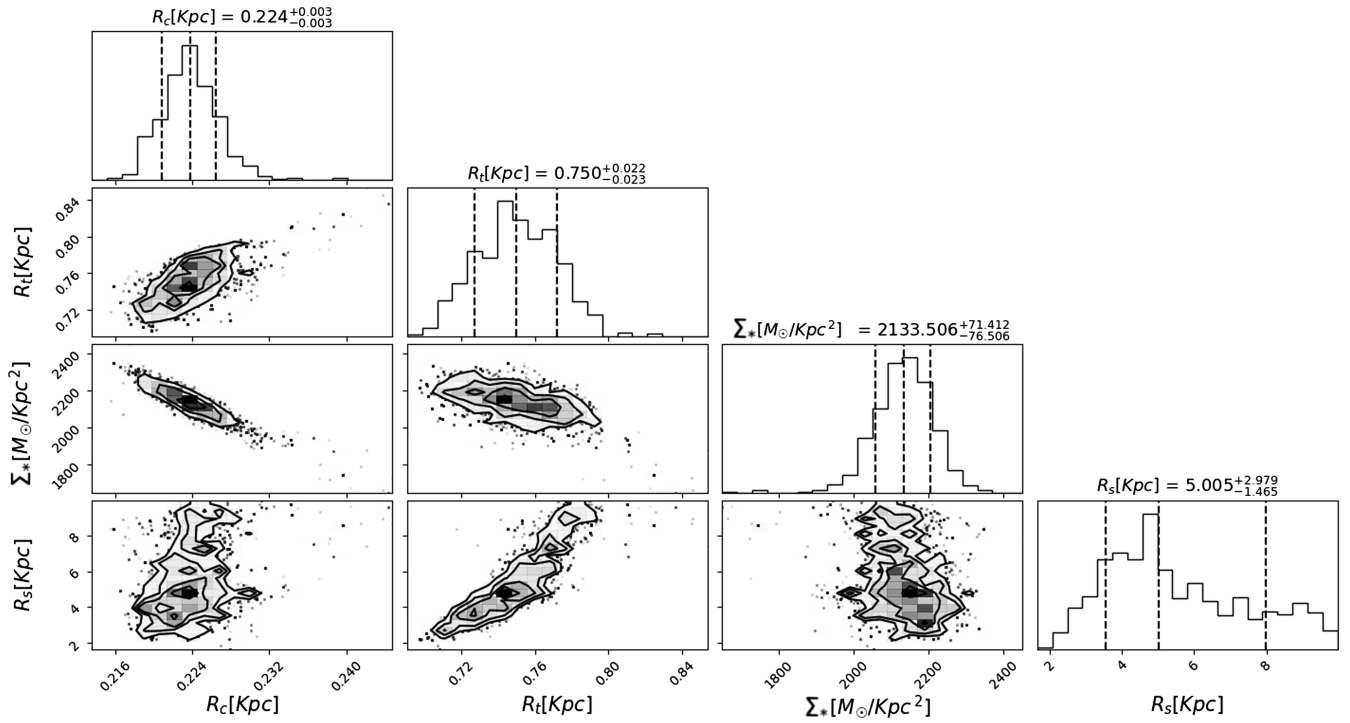
FIG. 31. Milky Way's dSph mean (Fig. 26 top panel): Correlated distributions of the free parameters. As can be seen the core radius and transition radius are well-defined despite the Gaussian input priors, indicating a reliable result. The contours represent the 68%, 95%, and 99% confidence levels. The best-fit parameter values are the medians (with errors), represented by the dashed black ones, and tabulated in Table I.

4. Andromeda

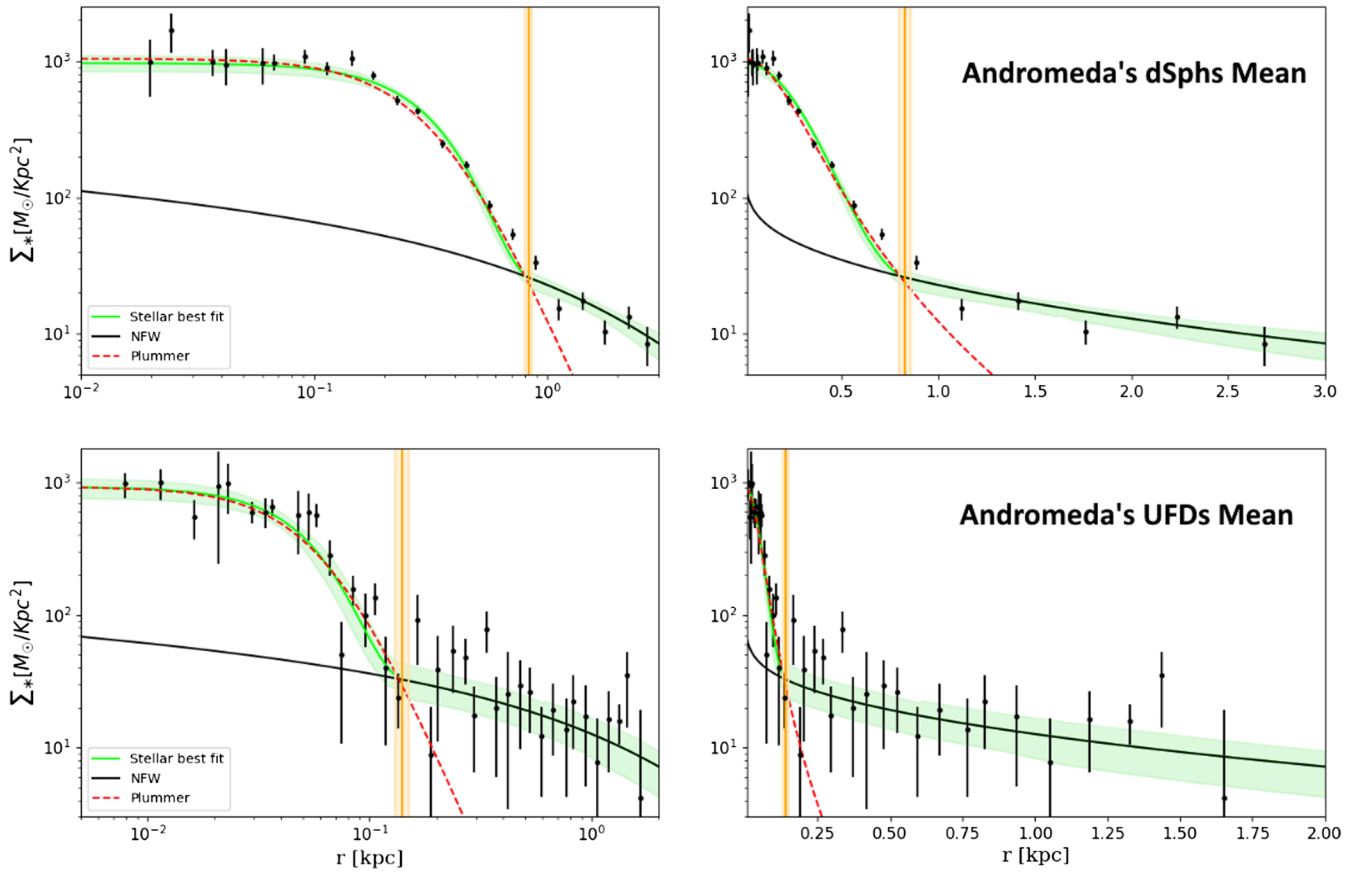Andromeda's galaxies alone.

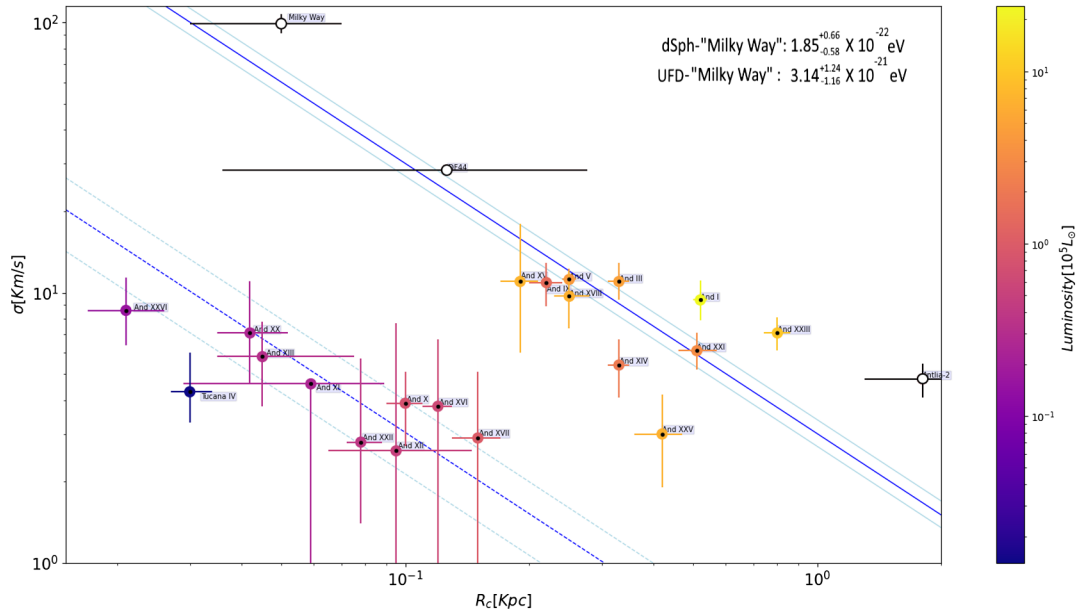FIG. 32.   Like Fig. 2 but just for Andromeda's satellites.

FIG. 33.   Velocity dispersion vs core radius: Like Fig. 3 but just for Andromeda's satellites.
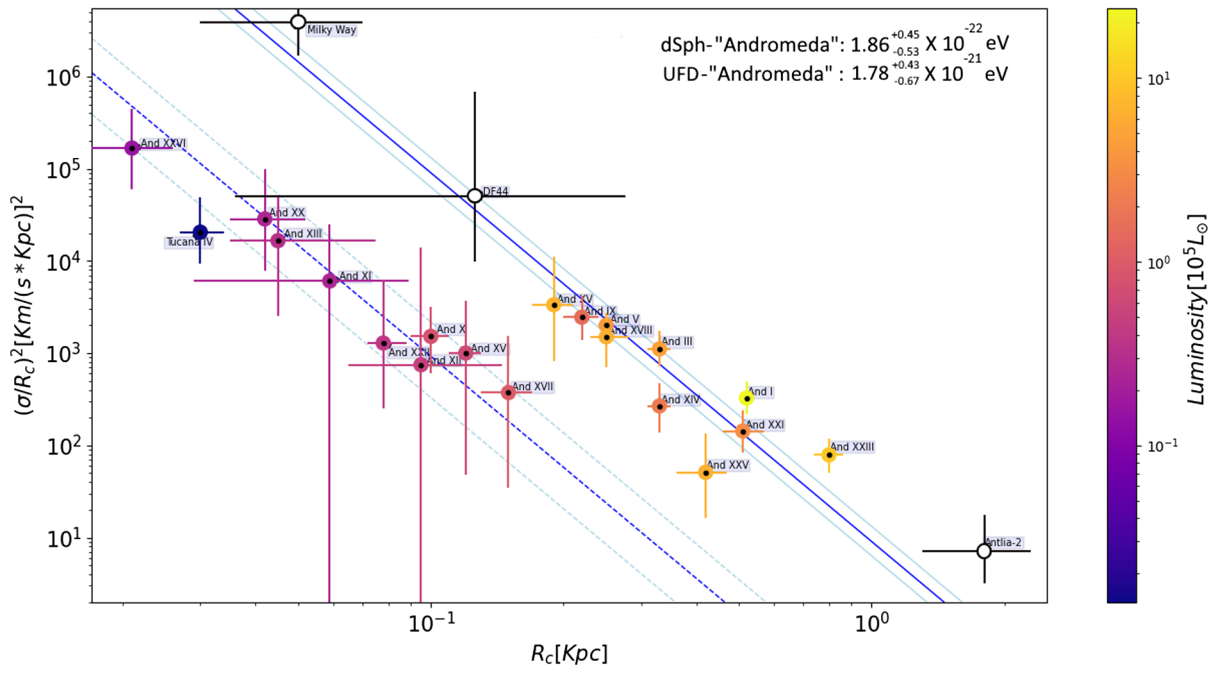
FIG. 34. DM density vs core radius: Like Fig. 1 but just for Andromeda's satellites.
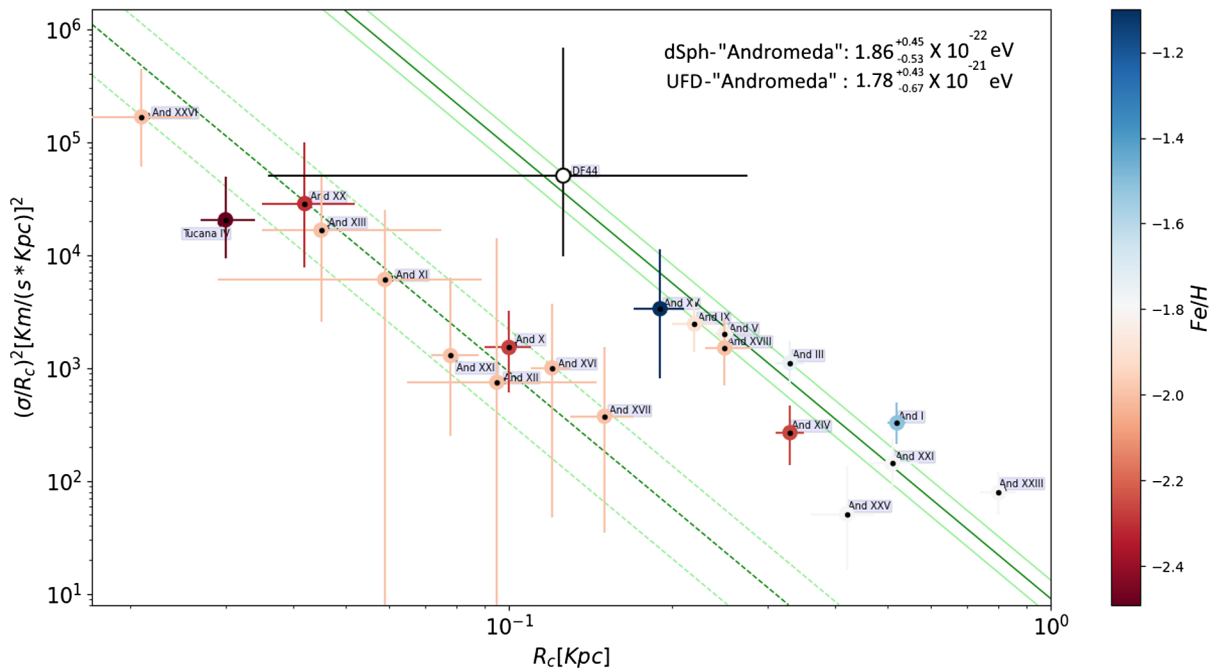

FIG. 35. DM density vs core radius: Like Fig. 5 but just for Andromeda's satellites.
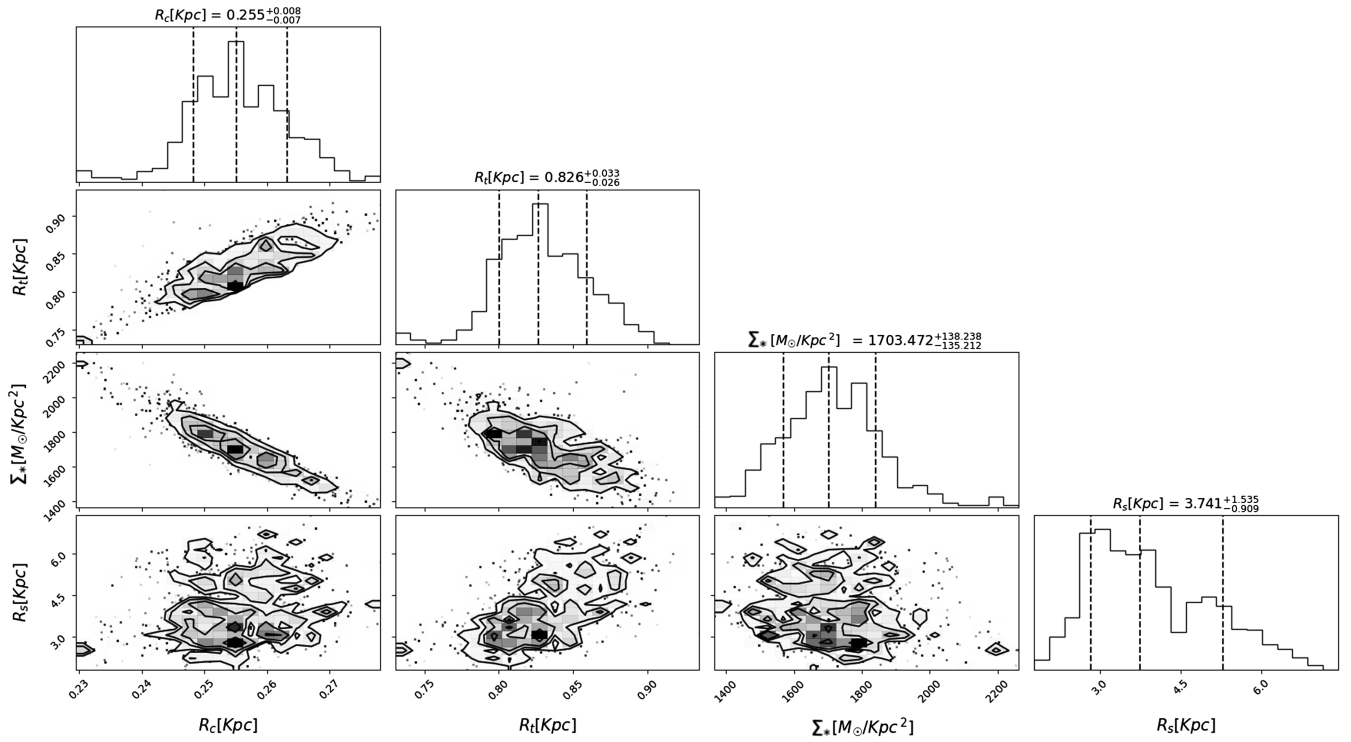
FIG. 36. Andromeda's dSph mean (Fig. 26 lower panel): Correlated distributions of the free parameters. As can be seen the core radius and transition radius are well-defined despite the Gaussian input priors, indicating a reliable result. The contours represent the 68%, 95%, and 99% confidence levels. The best-fit parameter values are the medians (with errors), represented by the dashed black ones, and tabulated in Table I.

FIG. 37. Andromeda's UFD mean (Fig. 26 lower panel): Correlated distributions of the free parameters. As can be seen the core radius and transition radius are well-defined despite the Gaussian input priors, indicating a reliable result. The contours represent the 68%, 95%, and 99% confidence levels. The best-fit parameter values are the medians (with errors), represented by the dashed black ones, and tabulated in Table I.
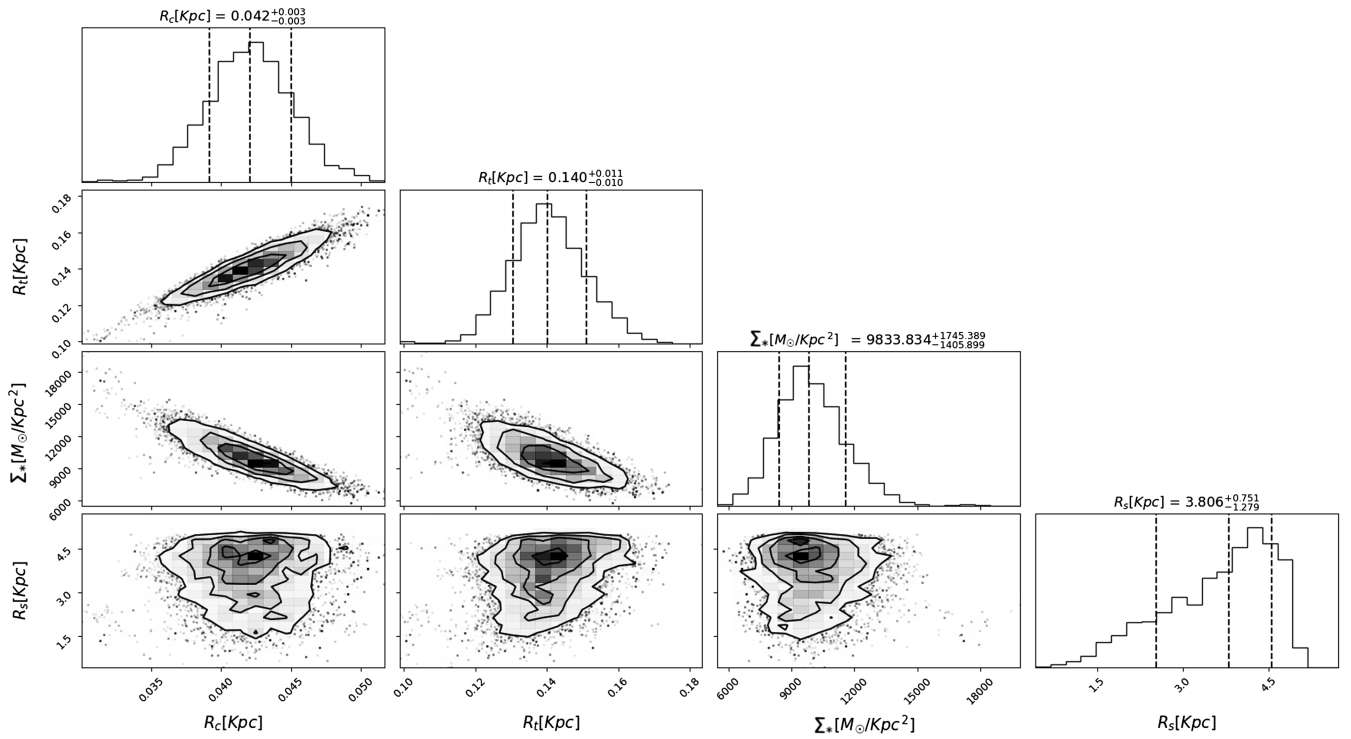
[1] Planck Collaboration, Planck 2018 results. VI. Cosmological parameters, Astron. Astrophys. **641**, A6 (2018).

[2] E. Aprile *et al.*, Dark matter search results from a one tonyear exposure of xenon1t, Phys. Rev. Lett. **121**, 111302 (2018).

[3] CMS Collaboration, Search for high mass dijet resonances with a new background prediction method in protonproton collisions at $\sqrt{s} = 13$ tev, J. High Energy Phys. 05 (2020) 033.

[4] B. Moore, Evidence against dissipation-less dark matter from observations of galaxy haloes, Nature (London) **370**, 629 (1994).

[5] W. J. G. de Blok, The core-cusp problem, Adv. Astron. **2020**, 789293 (2010).

[6] D. J. E. Marsh and A.-R. Pop, Axion dark matter, solitons and the cusp-core problem, Mon. Not. R. Astron. Soc. **451**, 2479 (2015).

[7] A. Klypin, A. V. Kravtsov, F. Valenzuela, and O. Prada, Where are the missing galactic satellites?, Astrophys. J. **522**, 82 (1999).

[8] M. Safarzadeh and A. Loeb, A new challenge for dark matter models, arXiv:2107.03478.

[9] S. Kim, A. H. G. Peter, and J. Hargis, Missing satellites problem: Completeness corrections to the number of satellite galaxies in the milky way are consistent with cold dark matter predictions, Phys. Rev. Lett. **121**, 211302 (2018).

[10] L. M. Widrow and N. Kaiser, Using the schroedinger equation to simulate collisionless matter, Astrophys. J. **416**, L71 (1993).

[11] W. Hu, R. Barkana, and A. Gruzinov, Fuzzy cold dark matter: The wave properties of ultralight particles, Phys. Rev. Lett. **85**, 1158 (2000).

[12] H.-Y. Schive, T. Chiueh, and T. Broadhurst, Cosmic structure as the quantum interference of a coherent dark wave, Nat. Phys. **10**, 496 (2014).

[13] L. Hui, A. Joyce, X. Landry, and M. J. Li, Vortices and waves in light dark matter, J. Cosmol. Astropart. Phys. 01 (2021) 011.

[14] H.-Y. Schive, M.-H. Liao, T.-P. Woo, S.-K. Wong, T. Chiueh, T. Broadhurst, and W-Y. Pauchy Hwang, Understanding the core-halo relation of quantum wave dark matter from 3D simulations, Phys. Rev. Lett. **113**, 261302 (2014).

[15] P. Mocz, M. Vogelsberger, V. H. Robles, J. Zavala, M. Boylan-Kolchin, A. Fialkov, and L. Hernquist, Galaxy formation with becdm—I. Turbulence and relaxation of idealized haloes, Mon. Not. R. Astron. Soc. **471**, 4559 (2017).

[16] J. Veltmaat, J. C. Niemeyer, and B. Schwabe, Formation and structure of ultralight bosonic dark matter halos., Phys. Rev. D **98**, 043509 (2018).

[17] J. C. Niemeyer, Small-scale structure of fuzzy and axionlike dark matter, Prog. Part. Nucl. Phys. **113**, 103787 (2020).

[18] P. Mocz *et al.*, First star-forming structures in fuzzy cosmic filaments, Phys. Rev. Lett. **123**, 141301 (2019).

[19] P. Mocz *et al.*, Galaxy formation with BECDM—II. Cosmic filaments and first galaxies, Mon. Not. R. Astron. Soc. **494**, 2027 (2020).

[20] J. Navarro and C. S. Frenk, The structure of cold dark matter halos, Astrophys. J. **462**, 563 (1996).

[21] M. R. Lovell, C. S. Frenk, V. R. Eke, A. Jenkins, L. Gao, and T. Theuns, The properties of warm dark matter haloes, Mon. Not. R. Astron. Soc. **439**, 300 (2014).

[22] B. Schwabe, J. C. Niemeyer, and J. F. Engels, Simulations of solitonic core mergers in ultralight axion dark matter cosmologies, Phys. Rev. D **94**, 043513 (2016).

[23] J. I. Read and G. Gilmore, Mass loss from dwarf spheroidal galaxies: The origins of shallow dark matter cores and exponential surface brightness profiles, Mon. Not. R. Astron. Soc. **356**, 107 (2005).

[24] N. C. Amorisco, A. Agnello, and N. W. Evans, The core size of the Fornax dwarf spheroidal, Mon. Not. R. Astron. Soc. **429**, L89 (2013).

[25] A. Pozo *et al.*, Galaxy formation with wave/fuzzy dark matter: The core-halo structure, arXiv:2310.12217.

[26] A. Chiti, A. Frebel, J. D. Simon, D. Erkal, L. J. Chang, L. Necib, A. P. Ji, H. Jerjen, D. Kim, and J. E. Norris, An extended halo around an ancient dwarf galaxy, Nat. Astron. **5**, 392 (2021).

[27] M. L. Collins, J. I Read, R. A Ibata, R. M. Rich, N. F. Martin, J. Peñarrubia, S. C Chapman, E. J Tollerud, and D. R. Weisz, Andromeda XXI—a dwarf galaxy in a low density dark matter halo, Mon. Not. R. Astron. Soc. **505**, 5686 (2021).

[28] I. de Martino, T. Broadhurst, S. H. Henry Tye, T. Chiueh, and H.-Y. Schive, Dynamical evidence of a solitonic core of $10^9 M_\odot$, Phys. Dark Universe **491**, 100503 (2020).

[29] A. Pozo, T. Broadhurst, I. de Martino, H. N. Luu, G. F. Smoot, J. Lim, and M. Neyrinck, Wave dark matter and ultradiffuse galaxies, Mon. Not. R. Astron. Soc. **504**, 2868 (2021).

[30] P. van Dokkum, A. Wasserman, S. Danieli, R. Abraham, J. Brodie, C. Conroy, D. A. Forbes, C. Martin, M. Matuszewski, A. J. Romanowsky, and A. Villaume, Spatially resolved stellar kinematics of the ultra-diffuse galaxy dragonfly 44. I Observations, kinematics, and cold dark matter halo fits, Astrophys. J. **880**, 91 (2019).

[31] M. G. Walker, M. Mateo, E. W. Olszewski, J. Peñarrubia, N. W. Evans, and G. Gilmore, A universal mass profile for dwarf spheroidal galaxies?, Astrophys. J. **704**, 1274 (2009).

[32] S.-R. Chen, H.-Y. Schive, and T. Chiueh, Jeans analysis for dwarf spheroidal galaxies in wave dark matter, Mon. Not. R. Astron. Soc. **468**, 1338 (2017).

[33] I. Della Monica, R. andde Martino, and T. Broadhurst, Explaining the oblate morphology of dwarf spheroidals with wave dark matter perturbations, arXiv:2308.14664.

[34] H. Huang, H.-Y. Schive, and T. Chiueh, Cosmological simulations of two-component wave dark matter, Mon. Not. R. Astron. Soc. **522**, 515 (2023).

[35] N. L. *et al.*, Nested solitons in two-field fuzzy dark matter, arXiv:2010.10337.

[36] M. Gosenca, A. Eberhardt, Y. Wang, B. Eggemeier, E. Kendall, J. Luna Zagorac, and R. Easther, Multifield ultralight dark matter, Phys. Rev. D **107**, 083014 (2023).

[37] L. Hui, Ultralight scalars as cosmological dark matter, Phys. Rev. D **95**, 043541 (2020).

[38] A. Arvanitaki, S. Dimopoulos, S. Dubovsky, N. Kaloper, and J. March-Russell, String axiverse, Phys. Rev. D **81**, 123530 (2010).

[39] H. N. Luu, S. H. H. Tye, and T. Broadhurst, Multiple ultralight axionic wave dark matter and astronomical structures, Phys. Dark Universe **30,** 100636 (2020).

[40] S. Mohammadtaher and D. N. Spergel, Ultra-light dark matter is incompatible with the milky way's dwarf satellites, Astrophys. J. **893,** 6 (2020).

[41] E. Armengaud, N. Palanque-Delabrouille, Christophe Yèche, D. J. E. Marsh, and J. Baur, Constraining the mass of light bosonic dark matter using SDSS Lyman-α forest, Mon. Not. R. Astron. Soc. **471,** 4606 (2017).

[42] Y.-H. Hsu and T. Chiueh, Evolution of perturbation and power spectrum in a two-component ultralight axionic universe, Phys. Rev. D **103,** 103516 (2021).

[43] V. Sahni and L. Wang, New cosmological model of quintessence and dark matter, Phys. Rev. D **62,** 103517 (2000).

[44] D. J. E. Marsh and J. Silk, A model for halo formation with axion mixed dark matter, Mon. Not. R. Astron. Soc. **437,** 2652 (2014).

[45] B. Bozek, J. Marsh, D. J. E. Silk, and R. F. G. Wyse, Galaxy UV-luminosity function and reionization constraints on axion dark matter, Mon. Not. R. Astron. Soc. **450,** 209 (2015).

[46] V. H. Robles, J. S. Bullock, and M. Boylan-Kolchin, Scalar field dark matter: Helping or hurting small-scale problems in cosmology?, Mon. Not. R. Astron. Soc. **483,** 289 (2019).

[47] J. Vicens, J. Salvado, and J. Miralda-Escudé, Bosonic dark matter halos: Excited states and relaxation in the potential of the ground state, arXiv:1802.10513.

[48] I. de Martino, T. Broadhurst, S. H. H. Tye, T. Chiueh, H.-Y. Schive, and R. Lazkoz, Recognising axionic dark matter by compton and de-Broglie scale modulation of pulsar timing, Phys. Rev. Lett. **119,** 221103 (2017).

[49] T. P. Woo and T. Chiueh, High-resolution simulation on structure formation with extremely light bosonic dark matter, Astrophys. J. **697,** 850 (2009).

[50] J. Binney and S. Tremaine, *Galactic Dynamics: Second edition* (Princeton University Press, New Jersey, 2008), https://press.princeton.edu/books/paperback/9780691130279/galactic-dynamics.

[51] A. L. Gregory, M. L. M. Collins, J. I. Read, M. J. Irwin, R. A. Ibata, N. F. Martin, A. W. McConnachie, and D. R. Weisz, Kinematics of the Tucana Dwarf Galaxy: An unusually dense dwarf in the Local Group, Mon. Not. R. Astron. Soc. **485,** 2010 (2019).

[52] A. W. McConnachie and M. J. Irwin, Structural properties of the M31 dwarf spheroidal galaxies, Mon. Not. R. Astron. Soc. **365,** 1263 (2006).

[53] A. W. McConnachie, N. Arimoto, M. Irwin, and E. Tolstoy, The stellar content of the isolated transition dwarf galaxy DDO210, Mon. Not. R. Astron. Soc. **373,** 715 (2006).

[54] M. I. Wilkinson, J. T. Kleyna, N. W. Evans, G. F. Gilmore, M. J. Irwin, and E. K. Grebel, Kinematically cold populations at large radii in the Draco and Ursa Minor dwarf spheroidal galaxies, Astrophys. J. **611,** L21 (2004).

[55] S. Sohn, S. R. Majewski, R. R. Munoz, W. E. Kunkel, K. V. Johnston, J C. Ostheimer, P. Guhathakurta, R. J. Patterson, M. H. Siegel, and M. C. Cooper, Exploring halo substructure with giant stars. X. Extended dark matter or tidal disruption?: The case for the Leo I dwarf spheroidal galaxy, Astrophys. J. **663,** 960 (2007).

[56] G. Battaglia, M. Rejkuba, E. Tolstoy, M. J. Irwin, and G. A. Beccari, A wide-area view of the phoenix dwarf galaxy from very large telescope/FORS imaging, Mon. Not. R. Astron. Soc. **424,** 1113 (2012).

[57] S. Okamoto et al., Population gradient in the Sextans dSph: Comprehensive mapping of a dwarf galaxy by Suprime-Cam, Mon. Not. R. Astron. Soc. **467,** 208 (2017).

[58] G. Torrealba, S. E. Koposov, V. Belokurov, and M. Irwin, The feeble giant. Discovery of a large and diffuse Milky Way dwarf galaxy in the constellation of crater, Mon. Not. R. Astron. Soc. **459,** 2370 (2016).

[59] P. M. Frinchaboy et al., A 2mass all-sky view of the sagittarius dwarf galaxy. VII. Kinematics of the main body of the sagittarius dSph, Astrophys. J. **756,** 74 (2012).

[60] D. Martínez-Delgado, J. Alonso-García, A. Aparicio, and M. A. Gómez-Flechoso, A tidal extension in the Ursa Minor dwarf spheroidal galaxy, Astrophys. J. **549,** L63 (2001).

[61] D. B. Zucker et al., A new Milky Way dwarf satellite in Canes Venatici, Astrophys. J. **643,** L103 (2006).

[62] A. G. Moskowitz and M. G. Walker, Stellar density profiles of dwarf spheroidal galaxies, Astrophys. J. **892,** 27 (2020).

[63] E. Saremi, A. Javadi, J. Th. van Loon, H. Khosroshahi, A. Molaeinezhad, I. McDonald, M. Raouf, A. Danesh, J. R. Bamber, P. Short, L. Suárez-Andrés, R. Clavero, and G. Gozaliasl, The Isaac Newton Telescope monitoring survey of local group dwarf galaxies. I. Survey overview and first results for andromeda I, Astrophys. J. **894,** 135 (2020).

[64] N. F. Martin et al., The PAndAS view of the andromeda satellite system. II. Detailed properties of 23 M31 dwarf spheroidal galaxies, Astrophys. J. **833,** 167 (2016).

[65] M. E. Spencer, M. Mateo, M. G. Walker, and E. W. Olszewski, A multi-epoch kinematic study of the remote dwarf spheroidal galaxy Leo II, Astrophys. J. **836,** 202 (2017).

[66] M. I. Wilkinson et al., Probing the dark matter content of local group dwarf spheroidal galaxies with flames, The Messenger **124,** 25 (2006).

[67] M. Fabrizio et al., The Carina project. X. On the kinematics of old and intermediate-age stellar populations, Astrophys. J. **830,** 126 (2016).

[68] A. B. Pace, M. Kaplinghat, E. Kirby , J. D Simon, E. Tollerud, R. R Muñoz, P. Côté, S. G. Djorgovski, and M. Geha, Multiple chemodynamic stellar populations of the Ursa Minor dwarf spheroidal galaxy, Mon. Not. R. Astron. Soc. **495,** 3022 (2020).

[69] S. Taibi, G. Battaglia, M. Rejkuba, R. Leaman, N. Kacharov, G. Iorio, P. Jablonka, and M. Zoccali, The Tucana Dwarf Spheroidal Galaxy: Not such a massive failure after all, Astron. Astrophys. **635,** A152 (2020).

[70] S. Taibi et al., Stellar chemo-kinematics of the Cetus dwarf spheroidal galaxy, Astron. Astrophys. **618,** A122 (2018).

[71] L. Hermosa Muñoz et al., Kinematic and metallicity properties of the aquarius dwarf galaxy from FORS2 MXU spectroscopy, Astron. Astrophys. **634,** A10 (2017).

[72] E. N. Kirby *et al.*, A chemistry and kinematics of the late-forming dwarf irregular galaxies leo A, aquarius, and sagittarius DIG, Astrophys. J. **834,** 9 (2017).

[73] D. Massari *et al.*, Stellar 3d kinematics in the Draco dwarf spheroidal galaxy, Astron. Astrophys. **633,** A36 (2020).

[74] A. W. McConnachie and K. A. Venn, Revised and new proper motions for confirmed and candidate Milky Way dwarf galaxies, Astron. J. **160,** 124 (2020).

[75] E. L. Łokas, G. A. Mamon, and F. Prada, Dark matter distribution in the Draco dwarf from velocity moments, Mon. Not. R. Astron. Soc. **363,** 918 (2005).

[76] A. Aparicio, R. Carrera, and D. Martínez-Delgado, The star formation history and morphological evolution of the Draco dwarf spheroidal galaxy, Astron. J. **122,** 2524 (2001).

[77] G. Battaglia, S. Taibi, G. F. Thomas, and T. K. Fritz, Gaia early DR3 systemic motions of Local Group Dwarf galaxies and orbital properties with a massive large Magellanic Cloud, Astron. Astrophys. **657,** A54 (2022).

[78] A. Koch, M. I. Wilkinson, J. T. Kleyna, G. F. Gilmore, E. K. Grebel, A. Dougal Mackey, N. W.Evans, R. F. G. Wyse and, Stellar kinematics and metallicities in the Leo I dwarf spheroidal galaxy—wide-field implications for galactic evolution, Astrophys. J. **657,** 241 (2007).

[79] E. Held, I. Saviane, and Y. Momany, Stellar populations in the phoenix dwarf galaxy, Astron. Astrophys. **345,** 747 (1999).

[80] D. R. Matus Carrillo, M. Fellhauer, A. G. Alarcon Jara, C. A. Aravena, and F. Urrutia Zapata, Modelling the Canes Venatici I dwarf spheroidal galaxy, Astron. Astrophys. **633,** A91 (2020).

[81] G. Battaglia, Study of the Sextans dwarf spheroidal galaxy from the DART Ca II triplet survey, Mon. Not. R. Astron. Soc. **411,** 1013 (2011).

[82] N. Caldwell, M. G. Walker, M. Mateo, E. W. Olszewski, S. Koposov, V. Belokurov, G. Torrealba, A. Geringer-Sameth, and C. I. Johnson, Crater 2: An extremely cold dark matter halo, Astrophys. J. **839,** 20 (2017).

[83] A. Koch, J. T. Kleyna, M. I. Wilkinson, E. K. Grebel, G. F. Gilmore, N. W. Evans, R F. G. Wyse, D. R. Harbeck, Stellar kinematics in the remote Leo II dwarf spheroidal galaxy-another brick in the wall, Astron. J. **134,** 566 (2007).

[84] K. Hayashi, M. Fabrizio, E. L Łokas, G. Bono, M. Monelli, M. Dall'Ora, and P. B Stetson, Dark halo structure in the Carina dwarf spheroidal galaxy: Joint analysis of multiple stellar components, Mon. Not. R. Astron. Soc. **481,** 250 (2018).

[85] T. J. L. de Boer *et al.*, The episodic star formation history of the Carina dwarf spheroidal galaxy, Astron. Astrophys. **572,** A10 (2014).

[86] R. Carrera, A. Aparicio, D. Martínez-Delgado, and J. Alonso-García, The star formation history and spatial distribution of stellar populations in the Ursa Minor dwarf spheroidal galaxy, Astron. J. **123,** 3199 (2002).

[87] M. Bettinelli, S. L. Hidalgo, S. Cassisi, A. Aparicio, G. Piotto, F. Valdes, and A. R. Walker, The star formation history of the Sculptor dwarf spheroidal galaxy, Mon. Not. R. Astron. Soc. **487,** 5862 (2019).

[88] E. N. Kirby *et al.*, Elemental abundances in M31: The kinematics and chemical evolution of dwarf spheroidal satellite galaxies, Astron. J. **159,** 46 (2020).

[89] M. L. M. Collins *et al.*, A kinematic study of the andromeda dwarf spheroidal system, Astrophys. J. **768,** 172 (2013).

[90] S. G. Alexander *et al.*, MOND calculations of bulk dispersions and radial dispersion profiles of Milky Way and andromeda dwarf spheroidal galaxies, Astrophys. J. **835,** 233 (2017).

[91] S. K. Jason *et al.*, The splash survey: Internal kinematics, chemical abundances, and masses of the andromeda I, II, III, VII, X, and XIV dwarf spheroidal galaxies, Astrophys. J. **711,** 671 (2010).

[92] A. W. McConnachie, The observed properties of dwarf galaxies in and around the local group, Astron. J. **144,** 4 (2012).

[93] S. McGaugh and M. Milgrom, Andromeda dwarfs in light of MOND. II. Testing prior predictions, Astrophys. J. **775,** 139 (2013).

[94] B. Mutlu-Pakdil, D. J. Sand, J. L. Carlin, K. Spekkens, N. Caldwell, D. Crnojević, A. K. Hughes, B. Willman, and D. Zaritsky, A deeper look at the new Milky Way satellites: Sagittarius II, reticulum II, phoenix II, and tucana III, Astrophys. J. **863,** 25 (2018).

[95] S. E. Koposov, V. Belokurov, G. Torrealba, and N. W. Evans, Beasts of the southern wild: Discovery of nine ultra faint satellites in the vicinity of the magellanic clouds, Astrophys. J. **805,** 130 (2015).

[96] S. E. Koposov *et al.*, Snake in the Clouds: A new nearby dwarf galaxy in the Magellanic bridge, Mon. Not. R. Astron. Soc. **479,** 5343 (2018).

[97] S. Okamoto, N. Arimoto, Y. Yamada, and M. Onodera, Stellar populations and structural properties of ultra faint dwarf galaxies, Canes Venatici I, Boötes I, Canes Venatici II, and Leo IV, Astrophys. J. **744,** 96 (2012).

[98] A. Chiti, A. Frebel, Alexander P. Ji, Mohammad K. Mardini, Xiaowei Ou, Joshua D. Simon, Helmut Jerjen, Dongwon Kim, and John E. Norris, Detailed chemical abundances of stars in the outskirts of the Tucana II ultrafaint dwarf galaxy, Astron. J. **165,** 55 (2023).

[99] M. J. Irwin, A. M. N. Ferguson, A. P. Huxor, N. R. Tanvir, R. A. Ibata, and G. F. Lewis, Andromeda XVII: A new low-luminosity satellite of M31, Astrophys. J. Lett. **676,** L17 (2008).

[100] S. C. Chapman *et al.*, Dynamics in the satellite system of Triangulum: Is And XXII a dwarf satellite of M33?, Mon. Not. R. Astron. Soc. **430,** 37 (2013).

[101] R. Muñoz, P. Côté, F. A. Santana, M. Geha, J. D. Simon, G. A. Oyarzún, P. B. Stetson, and S. G. Djorgovski, A MegaCam survey of outer halo satellites. III. Photometric and structural parameters, Astrophys. J. **860,** 66 (2018).

[102] D. Kim *et al.*, Portrait of a dark horse: A photometric and spectroscopic study of the ultra-faint milky way satellite pegasus III, Astrophys. J. **833,** 16 (2016).

[103] J. D. Simon *et al.*, Stellar kinematics and metallicities in the ultra-faint dwarf galaxy reticulum II, Astron. J. **808**, 95 (2015).

[104] S. A. o. Jenkins, Very large telescope spectroscopy of ultra-faint dwarf galaxies. I. Boötes I, Leo IV, and Leo V, Astrophys. J. **920**, 92 (2021).

[105] M. Blaña, M. Fellhauer, and R. Smith, Leo IV and V—a possible dwarf galaxy pair?, Astron. Astrophys. **542**, A61 (2021).

[106] J. D. Simon *et al.*, Birds of a feather? Magellan/IMACS spectroscopy of the ultra-faint satellites Grus II, Tucana IV, and Tucana V, Astrophys. J. **892**, 137 (2020).

[107] S. McGaugh and M. Milgrom, Andromeda dwarfs in light of MOND, Astrophys. J. **766**, 22 (2013).

[108] M. E. Putman *et al.*, The gas content and stripping of local group dwarf galaxies, Astrophys. J. **913**, 20 (2021).